Unconventional magnetic states and defects

Barts, Evgenii

DOI:
10.33612/diss.784926551

Chapter 4

Anisotropic exchange interactions in CrI_3

Abstract

Taming robust magnetism in two-dimensional(2D) materials is a promising avenue for novel applications by integrating it with electrical and optical methods. Ferromagnetic order in isotropic Heisenberg magnets is suppressed by spin fluctuations. It was, however, observed in a monolayer of CrI_3. This observation underscores the importance of anisotropic spin interactions in 2D van der Waals magnets. Here, we perform a symmetry analysis of the virtual electron hopping processes in CrI_3 in the regime of strong on-site Coulomb interactions and derive an anisotropic $JK\Gamma$ model describing effective spin interactions in this material [1] . The Heisenberg J and Kitaev K exchange interactions are derived in the model with strong spin-orbit coupling on ligand ions. We explain the absence of in-plane anisotropic exchange interaction Γ for an undistorted lattice using symmetry arguments and show that this term becomes non-zero even in absence of trigonal lattice distortions, if the electron hopping between ligand ions is taken into account. By developing a procedure that includes all emergent electron hopping paths, we calculate all symmetry-allowed spin-spin interactions between two arbitrary Cr ions, enabling us to obtain Heisenberg interactions between nearest-neighbor and next-nearest-neighbor Cr ions, as well as a large single-ion anisotropy. Our model shows that the dispersionless magnon energy gap observed in CrI_3 is primarily caused by the single-ion interactions, rather than by the Γ interaction. We also find that the next-nearest-neighbor Dzyaloshinskii-Moriya interaction is zero, suggesting that it is not a primary source of the topological gap at the Dirac point. Except for the Dirac point, the magnon spectrum predicted by our model is in good agreement with neutron scattering experimental data. These qualitative and quantitative findings for CrI_3 improve our understanding of complex magnetic behaviour in 2D materials and can be naturally generalized for other 2D magnets.

[1] Barts, E., Barone, P. & Mostovoy, M. Anisotropic exchange interactions in CrI_3, to be published.

4.1 Introduction

Two-dimensional van der Waals materials provide a unique playground for electric and optical control of many-electron systems [132], especially up-and-coming due to the recently discovered magnetic order in some of them [133–135]. Examples of van der Waals magnets are Cr-based trihalides: $CrCl_3$, $CrBr_3$, and CrI_3 [136]. In these materials, Cr^{3+} ions ($S = 3/2$) form weakly coupled two-dimensional honeycomb spin lattices. CrI_3 stands out due to its heavy I^- ions with a strong spin-orbit coupling (SOC) that octahedrally coordinate Cr ions [137]. Similarly to $RuCl_3$ with a strong SOC on magnetic sites, magnets with a strong SOC on ligand sites are promising candidates for physical realization of the Kitaev model with bond-dependent anisotropic exchange interactions hosting an exotic spin liquid state with anyonic excitations [138–141]. A single layer of CrI_3 shows a ferromagnetic order [142], which seemingly contradicts the Mermin-Wagner theorem prohibiting magnetic ordering in two dimensions. However, this theorem does not apply to anisotropic magnets. Bilayer CrI_3 shows an antiferromagnetic interplane coupling, and a variety of non-collinear states was predicted for its twisted version [143, 144]. Coexisting antiferromagnetic and ferromagnetic domains in the twisted bilayer have been experimentally observed recently [145]. Additionally, magnetic properties of CrI_3 can be tuned with applied electric fields [146–150]. These advances, promising for applications in spintronic devices [151, 152], heavily rely on the anisotropy of magnetic interactions in CrI_3.

The iodine ion has the large SOC ($\lambda_p = 0.63$ eV), which is the primary source of magnetic anisotropy in CrI_3 [153]. Despite the remarkable progress, there is still no agreement on the magnitude and origin of magnetic anisotropy, especially in the context of the magnon excitation spectrum [154, 155]. Magnons were shown to have a large energy gap at Dirac points [156], indicating the presence of topologically non-trivial bands [157, 158]. The so-called $JK\Gamma$ anisotropic model was used to describe the ferromagnetic resonance in CrI_3 [159]. On the other hand, recent inelastic neutron scattering experiments showed that the model with the next-nearest-neighbor Dzyaloshinskii-Moriya interaction (DMI) only is equally successful at describing the excitation spectra [160]. Moreover, the authors showed that in applied in-plane magnetic fields, the model with DMI gives a better quality fit but still does not explain all the features of the spectra.

Magnetic anisotropies induced by heavy ligand ions require a microscopic understanding beyond the symmetry-based phenomenological approach. Microscopically, the JK spin model was analytically derived in Ref. [161], and the off-diagonal Γ anisotropic term was shown to vanish for the ideal ligand octahedron. The authors also showed that trigonal distortions of the ligand octahedra induce the Γ term and, additionally, a single-ion anisotropy.

In this chapter, we microscopically derive the exchange interactions of the $JK\Gamma$

model in the *dp*-model, taking into account the SOC on iodine ions. Our results agree with those obtained in Ref. [161]. New to our work is a detailed symmetry analysis of hopping amplitudes demystifying the cancelation of the Γ coupling. We show that the anisotropic Γ interaction becomes non-zero for undistorted oxygen octahedra when an electron hopping between ligand ions is included. To understand the origin of the magnetic anisotropy, we design a procedure to obtain the effective Hamiltonian that describes all symmetry-allowed spin-spin interaction between two arbitrary Cr ions. This procedure accurately accounts for all emergent hopping paths due to electron hopping between iodines and includes pair-wise electron Coulomb interactions on ligand and metal ions. Using the available experimental and *ab initio* data on the microscopic parameters, we calculate exchange interactions between nearest-neighbor and next-nearest-neighbor Cr ions. Moreover, we obtain a non-zero second-order single-ion anisotropy, even in the absence of the trigonal distortions. All our findings are supported with symmetry analysis. Several features of the resulting magnon spectrum is in good agreement with the experimental data, which includes the uniform magnon energy gap at the Γ point and the magnon band widths of the optical and acoustic branches. Our main findings are that the single-ion anisotropy is the primary source of anisotropy at the Γ point, and the DMI between next-nearest-neighboring Cr ions is zero. Therefore, our model cannot explain the observed energy gap at the Dirac point.

This chapter is structured as follows. In Sec. 4.2, we derive the $JK\Gamma$ model. In Sec. 4.3, we introduce the general procedure to calculate spin-spin interactions between Cr ions, when *pp* hoppings between ligand ions is included. In Sec. 4.4, we apply this procedure to investigate DMI between next-nearest-neighboring Cr ions and provide symmetry arguments that explain its cancelation. We also discuss the origin of magnetic anisotropy at the Dirac point and the absence of a topological gap resulting from the DMI term. In Sec. 4.4, we perform the similar analysis at the Γ point of the magnon spectrum and calculate the effective second-order single-ion anisotropy, which we show to be the main source of magnetic anisotropy at this point. In Sec. 4.6, we analyze microscopic parameters, using available experimental and *ab initio* results, to calculate a realistic model that describe spin-spin interactions between nearest-neighbor and next-nearest-neighbor Cr ions. Using this model, we calculate magnon spectrum in CrI_3 and compare it with the experimentally observed spectrum. Finally, we conclude the chapter with Discussion section.

4.2 $JK\Gamma$ model

The electronic configuration of Cr^{3+} ions is $[Ar]4s^0 3d^3$ with half-filled t_{2g} orbitals: d_{xy}, d_{yz} and d_{xz}, whereas the empty e_g orbitals lie higher in energy due to crystal

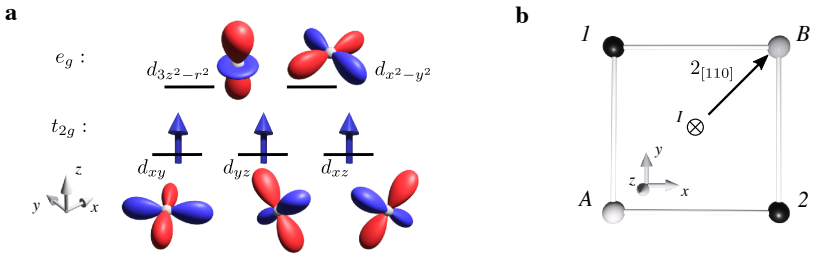

Figure 4.1: ***Electronic configuration of magnetic ions and bonds in*** CrI_3. **a** *The outer shell electrons of* Cr^{3+} *ion occupy three* t_{2g} *orbitals:* d_{xy}, d_{yz} *and* d_{xz}. *The* e_g *orbitals,* $d_{3z^2-r^2}$ *and* $d_{x^2-y^2}$, *are empty.* **b** *An ideal Cr-I plaquette. The white spheres depict* Cr^{3+} *ions, A and B. The black spheres depict* I^- *ions, 1 and 2. Symmetries of the plaquette are two two-fold rotation axes,* $2_{[110]}$ *and* 2_z, *with the inversion center at the center of the plaquette, I.*

field splitting (see Fig. 4.1 **a**). The symmetry of an ideal Cr-I plaquette includes two two-fold axes, $2_{[110]}$ and 2_z, and inversion (see Fig. 4.1 **b**) allowing for the spin exchange Hamiltonian,

$$\mathcal{H}_{NN} = J\boldsymbol{S}_A \cdot \boldsymbol{S}_B + KS_A^z S_B^z + \Gamma\left(S_A^x S_B^y + S_A^y S_B^x\right), \tag{4.1}$$

where $\boldsymbol{S}_{A,B}$ are the spin operators ($S = 3/2$), and x, y, z are the local plaquette coordinates. The first term in Eq. (4.1) is the isotropic Heisenberg exchange, the second term is the out-of-plane exchange anisotropy, and the last term is the symmetric in-plane exchange anisotropy. Note that the term $\Gamma_x\left(S_A^y S_B^z + S_A^z S_B^y\right) + \Gamma_y\left(S_A^z S_B^x + S_A^x S_B^z\right)$ with $\Gamma_x = -\Gamma_y$ by $2_{[110]}$ is not allowed by 2_z symmetry of the plaquette. These interactions result from the virtual delocalization of electrons in this Mott insulator. We derive the exchange interactions in Eq. (4.1) to the fourth-order of the perturbation theory in amplitudes of hopping between the metal d and ligand p orbitals.

4.2.1 Isotropic Heisenberg exchange J

The electron hopping between d_{yz} and d_{xz} orbitals of Cr ions A and B (see Fig. 4.2 **a**) involves two steps: the electron from the ligand p_z orbital hops into the d_{xz} orbital of the Cr-B ion leaving behind a hole subsequently filled with the electron from the d_{yz} orbital of the Cr-A ion. This process is only allowed for antiparallel spins of the two d electrons due to the Pauli exclusion principle and no spin-flip at the ligand. Thus, the energy of the state with antiparallel total spin projections of the two Cr ions $\left(S_z^A = -\frac{3}{2}, S_z^B = \frac{3}{2}\right)$ decreases by

$$E_{-\frac{3}{2},\frac{3}{2}} = -4\frac{t_{dd,1}^2}{U_1}, \tag{4.2}$$

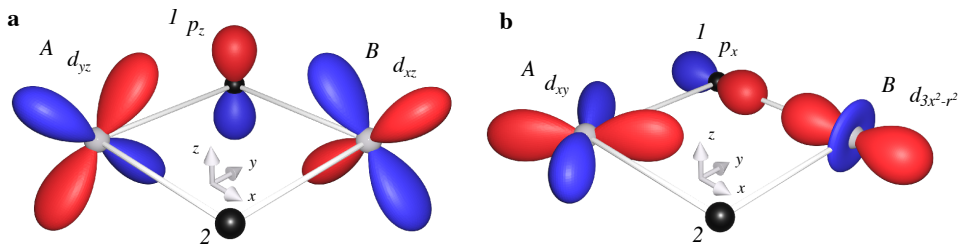

Figure 4.2: ***Ionic plaquette and hopping processes between nearest Cr ions****, with d orbitals of Cr-A and Cr-B and p orbitals of ligand ion 1 and 2 participating in the Heisenberg exchange processes.* **a** *An electron hops between the d_{yz} and d_{xz} orbitals via the p_z ligand orbital.* **b** *An electron hops between the d_{xy} and $d_{3x^2-r^2}$ orbitals via the p_x ligand orbital. The white (black) spheres show Cr^{3+} (I^-) ions. The red (blue) surfaces of constant density, $|\Psi(r)|^2$, depict positive (negative) orbital wave functions involved in the exchange processes.*

with the effective *dd*-hopping amplitude

$$t_{dd,S} = -\frac{t_{pd\pi}^2}{3}\left(\frac{2}{\Delta_S - \frac{\lambda}{2}} + \frac{1}{\Delta_S + \lambda}\right) \tag{4.3}$$

and a factor of two due to the hopping in the opposite direction (from Cr-B to Cr-A). An additional factor of two comes from the electron hopping via the second ligand. By $2_{[110]}T$ symmetry (180° rotation about the diagonal of the plaquette combined with time reversal), the energy contributions of the two exchange paths are equal. The effective hopping amplitude of spin-down electron moving from the d_{xz} orbital on site A to the d_{yz} on site B has the same absolute value: $t_{B,xz,\downarrow;A,yz,\downarrow} = (t_{B,yz,\downarrow;A,xz,\downarrow})^*$ (see Appendix 4.8.1 for details). U_S and Δ_S are the energies of intermediate states with an electron transferred to a Cr d orbital, at which 4 electrons are in the state with the total spin $S = 1, 2$. Δ_S is the charge transfer energy of the state with a hole in the iodine p shell and U_S is the on-site Coulomb repulsion in the state with two electrons on one Cr ion and 4 electrons on the other Cr ion. The expressions for U_S and Δ_S in terms of the dp model parameters are given in Appendix 4.8.3.

For the hopping between two t_{2g} orbitals, $S = 1$. The spin-orbit coupling at ligand ions only modifies the energies of intermediate states and does not make the exchange anisotropic:

$$\mathcal{H}_{\text{ex}} = \mathcal{H}_0 + J_{t_{2g}\to t_{2g}}(\mathbf{S}_A \cdot \mathbf{S}_B), \tag{4.4}$$

where

$$J_{t_{2g}\to t_{2g}} = \frac{8}{9}\frac{t_{dd,1}^2}{U_1}. \tag{4.5}$$

The exchange coupling is obtained by matching the energy difference for the parallel and antiparallel spin alignments with matrix elements of the Heisenberg Hamiltonian in Eq. (4.4), $J_{t_{2g}\to t_{2g}} = \frac{2}{9}\left(E_{\frac{3}{2},\frac{3}{2}} - E_{-\frac{3}{2},\frac{3}{2}}\right)$.

There is one more exchange path when an electron hops from the d_{xy} orbital of ion A into the d_{xy} orbital of ion B via the SOC-coupled p_x and p_y orbitals of a ligand ion. This process involves no spin-flip at the ligand ion, and its contribution is canceled by a similar process involving another ligand ion. This cancelation can be understood by applying $2_{[110]}T$ symmetry transformation to the hopping amplitude, which requires this amplitude to be real, $t_{B,xy,\downarrow;A,xy,\downarrow} = (t_{B,xy,\downarrow;A,xy,\downarrow})^*$, whereas the imaginary matrix element of the spin-orbit interaction between the p_x and p_y orbitals makes this amplitude purely imaginary. Hence, it is 0.

The virtual processes involving the hopping from t_{2g} orbitals of one Cr ion to e_g orbitals of another ion lead to an additional contribution to the isotropic exchange coupling,

$$J_{t_{2g}\to e_g} = -\frac{1}{3}\left(\frac{t_{pd\sigma}}{t_{pd\pi}}\right)^2\left(\frac{t_{dd,2}^2}{U_2} - \frac{t_{dd,1}^2}{U_1}\right). \tag{4.6}$$

In one of such processes, shown in Fig. 4.2 **b**, an electron hops from the p_x orbital of ligand 1 to the $d_{3x^2-r^2}$ orbital of Cr-B ion. As we take into account hopping via the second ligand (with hopping to the $d_{3y^2-r^2}$ orbital), the electron effectively hops only to the $d_{3z^2-r^2}$ orbital, since the hopping amplitudes to the $d_{x^2-y^2}$ orbital deconstructively interfere:

$$\begin{aligned} |d_{3x^2-r^2}\rangle &= -\frac{1}{2}|d_{3z^2-r^2}\rangle + \frac{\sqrt{3}}{2}\left|d_{x^2-y^2}\right\rangle, \\ \left|d_{3y^2-r^2}\right\rangle &= -\frac{1}{2}|d_{3z^2-r^2}\rangle - \frac{\sqrt{3}}{2}\left|d_{x^2-y^2}\right\rangle. \end{aligned} \tag{4.7}$$

Since the $d_{3z^2-r^2}$ orbital was empty, the intermediate state of the Cr-B ion with both $S = 1$ and $S = 2$ are allowed, and the states with both parallel and antiparallel spin alignments of the two Cr ions lower their energy due to this exchange process. For antiparallel spin projections, the energy is

$$E_{-\frac{3}{2},\frac{3}{2}} = -2\left(\frac{t_{pd\sigma}}{t_{pd\pi}}\right)^2\left(\frac{t_{dd,2}^2}{U_2}\frac{1}{4} + \frac{t_{dd,1}^2}{U_1}\frac{3}{4}\right). \tag{4.8}$$

The coefficients, $\frac{1}{4}$ for $S = 2$ and $\frac{3}{4}$ for $S = 1$, appear due to the expansion of the wave function describing the hopping of the spin-down electron to the Cr ion with the spin projection $+3/2$ over the eigenfunctions of the total spin of the four electrons in the intermediate state,

$$\left|\frac{1}{2},-\frac{1}{2}\right\rangle\left|\frac{3}{2},\frac{3}{2}\right\rangle = \frac{\sqrt{3}}{2}|1,1\rangle + \frac{1}{2}|2,1\rangle, \tag{4.9}$$

where the spin wave functions $|S, S_z\rangle$ in the right-hand side of the equations describe states with the total spin S and spin projection S_z. For parallel spins of the two Cr ions, the intermediate spin has $S = 2$, and the corresponding energy is

$$E_{\frac{3}{2},\frac{3}{2}} = -2\left(\frac{t_{pd\sigma}}{t_{pd\pi}}\right)^2 \frac{t_{dd,2}^2}{U_2}. \tag{4.10}$$

From Eqs. (4.9) and (4.10), we obtain the contribution of these processes to the Heisenberg exchange constant (see Eq. (4.6)).

To compare $J_{t_{2g}\to e_g}$ with the previous results in Ref. [161], we omit λ and expand denominators in the Hund coupling $J_{\rm H}$. Using $\Delta_2 = \Delta_1 - 4J_{\rm H}$ and $U_2 = U_1 - 4J_{\rm H}$, we obtain

$$J_{t_{2g}\to e_g} = -J_{\rm H}\frac{4t_{pd\sigma}^2 t_{pd\pi}^2}{3}\frac{1}{U_1 U_2 \Delta_2^2}\left(1 + \frac{2U_1}{\Delta_1}\right). \tag{4.11}$$

Comparing this result with that obtained in Ref. [161] under an assumption that Δ_S is not intermediate state dependent gives

$$\frac{J^{(\rm our)}_{t_{2g}\to e_g}}{J^{[161]}_{t_{2g}\to e_g}} = \left(1 + \frac{2U_1}{\Delta_1}\right). \tag{4.12}$$

In both calculations, the exchange processes involving tho holes on ligand ions are neglected, which requires the charge-transfer energy Δ_1 to be much larger than the Hubbard U_1. In this limit, U_1/Δ_1 in Eq. (4.12) is small.

The exchange constants in Eqs. (4.5) and (4.6) were obtained considering only two sets of spin projections of Cr ions. The result is valid for all spin projections, as is shown in Appendix 4.8.4 using Clebsch-Gordan coefficients.

4.2.2 Out-of-plane anisotropic exchange K

The value of the coupling constant K was calculated analytically and was found to be positive (corresponding to the antiferromagnetic anisotropic exchange) [161]. The sign of K is in agreement with DFT calculations [154] and is in disagreement with experimental fits of magnon [160] and FMR [159] spectra. The spin-orbit interaction on ligand ions gives rise to an effective *dd*-hopping amplitude with a spin flip accompanied by a change of orbital state of the ligand hole (see Appendix 4.8.5 for details). For example, a spin-up electron from the Cr-A d_{yz} orbital can hop into the d_{xy} orbital of Cr-B with spin down owing to the coupling between $p_y, \downarrow$ and $p_z, \uparrow$ states of the ligand 1 (see Fig. 4.3 **a**). Such processes lower the energy of the state with $+3/2$ projections

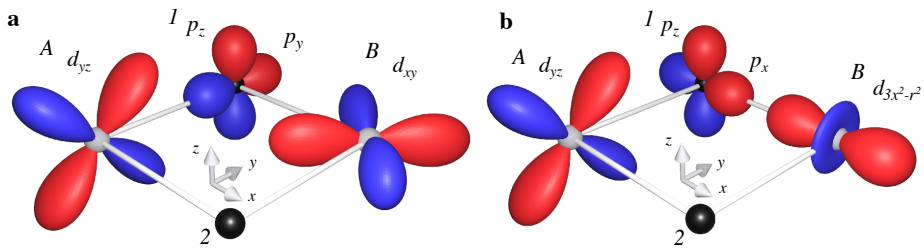

Figure 4.3: ***Ionic plaquette and hopping processes between nearest Cr ions with spin flip*** *with d orbitals of transition metal ions A and B and p orbitals of ligand ions 1 and 2 participating in the exchange processes with electron spin-flip.* **a** *An electron hops between the d_{yz} and d_{xy} orbitals via the SOC-entangled p_z and p_y ligand orbitals.* **b** *An electron hops between the d_{yz} and $d_{3x^2-r^2}$ orbitals via the SOC-entangled p_z and p_x ligand orbitals. The white (black) spheres show Cr^{3+} (I^-) ions. The red (blue) surfaces of constant density, $|\Psi(r)|^2$, depict positive (negative) orbital wave functions participating in the exchange process.*

of both Cr spins by

$$\begin{aligned} E_{\frac{3}{2},\frac{3}{2}} &= -8t_{pd\pi}^4 \left(\frac{1}{\Delta_1 - \frac{\lambda}{2}} \frac{1}{3} - \frac{1}{\Delta_1 + \lambda} \frac{1}{3} \right)^2 \frac{1}{U_1} \\ &= -8 \frac{(t_{dd(\mathrm{sf}),1})^2}{U_1}, \end{aligned} \tag{4.13}$$

where

$$t_{dd(\mathrm{sf}),S} = -\frac{\lambda t_{pd\pi}^2}{2(\Delta_S - \frac{\lambda}{2})(\Delta_S + \lambda)} \tag{4.14}$$

is the effective dd hopping amplitude with a spin flip for $S = 1, 2$. Since this virtual process does not change the spins of Cr ions, it leads to the Ising-like interaction,

$$\mathcal{H} = \mathcal{H}_0 + K_{t_{2g}\to t_{2g}} S_A^z S_B^z, \tag{4.15}$$

For Cr spins with opposite spin projections, $+3/2$ and $-3/2$, the energy decrease is zero, so that $K_{t_{2g}\to t_{2g}} = \frac{2}{9}\left(E_{\frac{3}{2},\frac{3}{2}} - E_{-\frac{3}{2},\frac{3}{2}}\right)$. An additional factor of two, compared to the expression for J, is due to the hopping from the d_{xy} orbital of the cation A via the coupled p_x and p_z ligand orbitals to the d_{xz} orbital of the cation B. These two amplitudes are related by $2_{[110]}T$ symmetry: $t_{B,xy,\uparrow;A,yz,\downarrow} = -i(t_{B,xy,\uparrow;A,xz,\downarrow})^*$. Summing up all such processes, we obtain

$$K_{t_{2g}\to t_{2g}} = -\frac{16}{9} \frac{(t_{dd(\mathrm{sf}),1})^2}{U_1}. \tag{4.16}$$

This value agrees with the result obtained in Ref. [161].

These Ising-like interactions also originate from the spin-flip hopping between the d_{yz} and $d_{3x^2-r^2}$ orbitals via the entangled p_x and p_z ligand orbitals (see Fig. 4.3 **b**). A calculation, similar to the calculation of $J_{t_{2g}\to e_g}$, yields

$$K_{t_{2g}\to e_g} = \frac{2}{3}\left(\frac{t_{pd\sigma}}{t_{pd\pi}}\right)^2\left(\frac{(t_{dd(\mathrm{sf}),2})^2}{U_2} - \frac{(t_{dd(\mathrm{sf}),1})^2}{U_1}\right). \tag{4.17}$$

The doubling here is due to

$$t_{B,3x^2-r^2,\downarrow;A,yz,\uparrow} = i(t_{B,3y^2-r^2,\downarrow;A,xz,\uparrow})^*, \tag{4.18}$$

required by $2_{[110]}T$ symmetry. To lowest order J_{H} and λ, we get

$$K_{t_{2g}\to e_g} = J_{\mathrm{H}}\frac{2}{3}\frac{t_{pd\sigma}^2 t_{pd\pi}^2\lambda^2}{\Delta_1^4 U_1 U_2}\left(1+\frac{4U_1}{\Delta_1}\right), \tag{4.19}$$

which, under an assumption that Δ_S is not intermediate state dependent, agrees with the previous result [161], except for the $4U_1/\Delta_1$ term that vanishes in the $\Delta_1\to\infty$ (dd Hubbard model) limit,

$$\frac{K^{(\mathrm{our})}_{t_{2g}\to e_g}}{K^{[161]}_{t_{2g}\to e_g}} = \left(1+\frac{4U_1}{\Delta_1}\right). \tag{4.20}$$

4.2.3 Off-diagonal exchange Γ

The Γ term in Eq. (4.1) was shown to be zero in the case of the ideal 90° Cr-I plaquette due to a subtle cancelation between the hopping paths via ligand ions 1 and 2, but it becomes non-zero when the trigonal deformation of the plaquette present in CrI_3 is taken into account [161]. We discuss the symmetry grounds behind this cancelation and show that this interaction is non-zero even for an undistorted plaquette if the hopping between ligand ions is included in the dp model Hamiltonian. To obtain a non-vanishing Γ term, we need imaginary effective dd hopping amplitudes, as can be seen from the fact that this spin-spin interaction has imaginary matrix elements, $(S_1^xS_2^y + S_1^yS_2^x) = \frac{i}{2}\left(S_1^-S_2^- - S_1^+S_2^+\right)$. The virtual electron hopping processes that lower (or increase) spin projections of both Cr ions are possible due to the SOC on ligand sites. One of them is similar to that contributing to $K_{t_{2g}\to e_g}$, shown in Fig. 4.3 **b**, but with an additional Hund's rule interaction in the intermediate state with four electrons on the Cr-B site. The spin projection of the hopping electron changes the sign three times: two times on the ligand site 1 (on the way from A to B and on the way back) and once on the B-site, which results in

$$\Gamma \sim i\left(\left(t_{B,\downarrow,3x^2-r^2;A,yz,\uparrow}\right)^2 - \left(t^*_{B,\downarrow,3x^2-r^2;A,yz,\uparrow}\right)^2\right), \tag{4.21}$$

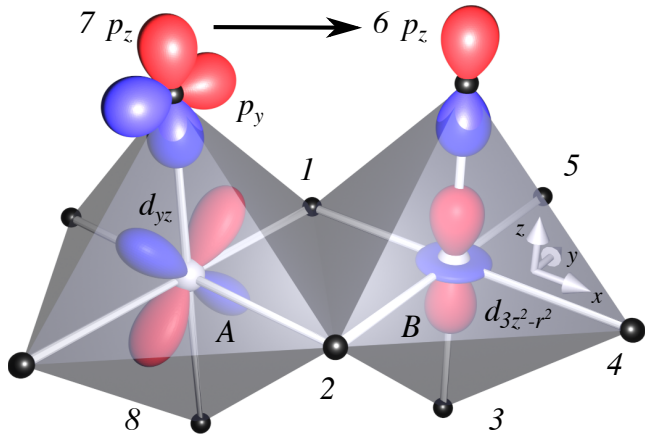

Figure 4.4: ***Two Cr and neighboring ligand ions and an electron hopping path via an apex ligand ion.*** *The arrow shows the direction of hopping between the p_z orbitals of ligand ions 6 and 7, resulting in an imaginary amplitude of the effective hopping between the d_{yz} to $d_{3z^2-r^2}$ orbitals. An electron hops from the p_z orbital of ligand 6 to the empty $d_{3z^2-r^2}$ orbital of Cr-B. Then the hole at ligand ion 6 is filled by the electron that hopped from the p_z orbital of ligand ion 7. Finally, the electron that occupied the d_{yz} orbital of Cr-A hops into the p_z orbital of ligand ion 7 via the p_y orbital and with the spin flip due to the spin-orbit coupling. The white (black) spheres show Cr^{3+} (I^-) ions. The red (blue) surfaces of constant density, $|\Psi(r)|^2$, depict positive (negative) orbital wave functions participating in the exchange process.*

where the second term comes from hopping to $d_{3y^2-r^2}$ from d_{xz} via the second ligand ion calculated using the symmetry relation Eq. (4.18). For the 90°-plaquette, the effective hopping amplitude $t_{B,\downarrow,3x^2-r^2;A,yz,\uparrow}$ is a real number (as discussed in Sec. 4.2.2), hence, the right-hand-side of Eq. (4.21) is zero. Trigonal distortions lead to additional hopping channels with imaginary amplitudes resulting in a non-zero Γ term linear in the distortion amplitude [161].

However, a sizable contribution to the Γ term occurs in the undistorted plaquette due to the hopping between ligand ions. This hopping amplitude is substantial for large $5p$ orbitals because of the large ionic radius of iodine ion (=2.2 Å) compared with that of Cr^{3+} ion (=0.615 Å) [163], even though the distance between nearest-neighbor ligand ions is $\sqrt{2}$ times larger than the one between Cr ions in the undistorted plaquette. The off-diagonal spin exchange coupling Γ is

$$\Gamma = \frac{1}{3}\left(3t_{pp\pi} - t_{pp\sigma}\right)\left(\frac{t_{pd\sigma}}{t_{pd\pi}}\right)^2\left(\frac{(t_{dd(\mathrm{sf}),2})^2}{U_2\Delta_2} - \frac{(t_{dd(\mathrm{sf}),1})^2}{U_1\Delta_1}\right), \tag{4.22}$$

to first order in $t_{pp\pi}$ and $t_{pp\sigma}$, which are the hopping amplitudes between the p orbitals

of two ligand ions (see Appendix 4.8.3). One of the processes contributing to Eq. (4.22) is the hybridization between apex ligand ions 6 and 7. Figure 4.4 shows the hopping path resulting in an imaginary effective *dd*-hopping amplitude, which to first order of the expansion in powers of λ is

$$\langle p_{y,7}\uparrow|\, H_{dp}\, |d_{yz,A}\uparrow\rangle\, \langle p_{z,7}\downarrow|\, H_{\rm SOC}\, |\, p_{y,7}\uparrow\rangle \langle p_{z,6}\downarrow|\, H_{pp}\, |\, p_{z,7}\downarrow\rangle \langle d_{3z^2-r^2,B}\downarrow|\, H_{dp}\, |\, p_{z,6}\downarrow\rangle, \tag{4.23}$$

where $p_{z,6}$ is the p_z orbital of ligand ion 6, and $d_{3z^2-r^2,B}$ is the $d_{3z^2-r^2}$ orbital of Cr-B. In this process, the spin-down electron hops from the $p_{z,6}$ orbital to the $d_{3z^2-r^2,B}$ orbital. The $p_{z,6}$ hole is filled by the electron from the $p_{z,7}$ orbital. The hole on ligand ion 7 changes its orbital state, followed by the spin flip due to the SOC-entangled $p_{z,6}$ and $p_{y,6}$ orbitals ($\langle p_{z,7}\downarrow|\, H_{\rm SOC}\, |\, p_{y,7}\uparrow\rangle \sim i\lambda$ (see Appendix 4.8.5). Then the electron occupying the $d_{yz,A}$ orbital hops into the $p_{y,7}$ orbital. The matrix element of this effective *dd*-hopping is purely imaginary. Hence, it gives rise to imaginary matrix element for an electron moving back and forth between the d orbitals of Cr-A and Cr-B when combined with the conventional *dd*-hopping in the reverse direction (see the discussion in Sec. 4.2.2). Importantly, degenerate perturbation theory in $t_{pp\pi}$ and λ is used to obtain Eq. (4.22), since the intermediate states with a single hole at a ligand have equal energies, while the *pp*-hopping matrix element given in Eq. (4.23) indicates the electron hopping path. To calculate energies of intermediate states, we diagonalized the Hamiltonian describing one hole delocalized over p-orbitals of two ligand ions, which includes the SOC (see Appendix 4.8.6). The resulting imaginary part of the effective amplitude of electron hopping from the $d_{yz,A}$ to the $d_{3z^2-r^2,B}$ orbital (see Eq. (4.23)), which is linear in $t_{pp\pi}$, $t_{pp\sigma}$ and λ, is

$$\mathrm{Im}\left(t_{B,\downarrow,3z^2-r^2;A,yz,\uparrow}\right) = t_{pd\sigma}\frac{(3t_{pp\pi}-t_{pp\sigma})\,\lambda}{4\Delta_S^3}\,(-t_{pd\pi})\,. \tag{4.24}$$

Here, $t_{pd\sigma}$ is the amplitude of the electron hopping from the $p_{z,6}$ orbital to the $d_{3z^2-r^2,B}$ orbital, the denominator is due to the intermediate state with the hole on the coupled p orbitals of ligand ions 6 and 7, and $(-t_{pd\pi})$ is the hopping amplitude between the $d_{yz,A}$ and the $p_{y,7}$ orbitals. The contribution to Eq. (4.22) from these hopping processes is obtained by matching the matrix element of lowering spin projections at both Cr sites (from 3/2 to 1/2), $\frac{3i}{2}\Gamma$, calculated in the $JK\Gamma$ model with that obtained in the dp model,

$$\begin{aligned} &i\mathrm{Im}\left(t_{B,\downarrow,3z^2-r^2;A,yz,\uparrow}\right)\frac{(-1)}{U_2}\mathrm{Re}\left(t_{A,yz,\downarrow;B,\uparrow,3x^2-r^2}\right)\left(-\frac{1}{2}\right)\frac{\sqrt{3}}{4} = \\ &i\mathrm{Im}\left(t_{B,\downarrow,3z^2-r^2;A,yz,\uparrow}\right)\frac{(-1)}{U_2}t_{pd\pi}\left(\frac{(-1)}{\Delta_2-\frac{\lambda}{2}}\sqrt{\frac{2}{3}}\frac{1}{\sqrt{6}}+\frac{(-1)}{\Delta_2+\lambda}\frac{1}{\sqrt{3}}\frac{(-1)}{\sqrt{3}}\right)\left(-\frac{t_{pd\sigma}}{2}\right)\frac{1}{\sqrt{3}}\frac{\sqrt{3}}{4}. \end{aligned} \tag{4.25}$$

The second line in Eq. (4.25) describes the electron moving back with the spin-flip via the $p_{x,1}$ and $p_{z,1}$ orbitals to the $d_{yz,A}$ orbital. Since the electron hops back from the $d_{3x^2-r^2,B}$ orbital, there is an additional factor of $-1/2$ due to the overlap between the $d_{3x^2-r^2,B}$ and $d_{3z^2-r^2,B}$ orbitals, $|d_{3x^2-r^2}\rangle = -\frac{1}{2}|d_{3z^2-r^2}\rangle + \frac{\sqrt{3}}{2}\left|d_{x^2-y^2}\right\rangle$. The spin-down electron hopping into the $d_{3x^2-r^2,B}$ orbital and returning with spin-up into the spin state $S = 2$, which lowers the spin projection at Cr-B site. Therefore, the factor of $\sqrt{3}/4$ in Eq. (4.25) is a cross-term in the Clebsch-Gordan decomposition of the four-electron intermediate spin state, $|S, S_z\rangle$:

$$|2,1\rangle = \frac{1}{2}\downarrow\left|\frac{3}{2},\frac{3}{2}\right\rangle + \frac{\sqrt{3}}{2}\uparrow\left|\frac{3}{2},\frac{1}{2}\right\rangle, \tag{4.26}$$

where the arrow is the spin projection of the hopping electron, and the ket-state on the right side of the equality is the spin state of three electrons on Cr-B. For the spin state $S = 1$, the contribution to the matrix element the form similar to Eq. (4.25) but with Δ_1 and U_1 and the opposite sign, since

$$|1,1\rangle = \frac{\sqrt{3}}{2}\downarrow\left|\frac{3}{2},\frac{3}{2}\right\rangle - \frac{1}{2}\uparrow\left|\frac{3}{2},\frac{1}{2}\right\rangle. \tag{4.27}$$

The last factor of $1/\sqrt{3}$ in Eq. (4.25) is from the final state projection onto the $\left|\frac{3}{2},\frac{1}{2}\right\rangle$ state on A site. Equation (4.25) is multiplied by the factor of 8 to obtain the final expression for the Γ term in Eq. (4.22) that accounts for the $p_{x,7} - p_{x,6}$ hybridization with the spin-flip hopping through the $p_{y,2} - p_{z,2}$ orbitals to $d_{xz,A}$ and for the hopping sequence (when an electron first hops to an e_g orbital of Cr-B via the ligand 1). Importantly, the hybridization between ligand ions 3 and 8 does not cancel the contribution due to two sign changes in the matrix elements of the hopping from the $p_{y,8}$ to $d_{yz,A}$ orbital and from the $p_{z,3}$ to $d_{3z^2-r^2,B}$ orbital compared to Eq. (4.23):

$$\langle p_{y,8}\uparrow|\, d_{yz,A}\uparrow\rangle\langle p_{z,8}\downarrow|\, p_{y,8}\uparrow\rangle\langle p_{z,3}\downarrow|\, p_{z,8}\downarrow\rangle\langle d_{3z^2-r^2,B}\downarrow|\, p_{z,3}\downarrow\rangle. \tag{4.28}$$

However, the hybridization between ligand ions 8 and 3 do not double the contribution, since in the secular equation for the energies of the coupled p orbitals, resulting wave functions come with the normalization factor, e.g. $1/\sqrt{2}$ for two states only.

Note that the processes involving the hybridization of one of the plaquette ligand ions (1 or 2 in Fig.4.4) with any other ligand ions deconstructively interfere, hence, giving no contribution to the Γ term linear in the pp-hopping. For example, the contribution from the electron hopping via the p-orbitals of ligand ions 1 and 2 is canceled by the contribution from the ligand ions 1 and 5. These matrix elements involve the same hopping amplitudes between ligand ions:

$$\langle p_{y,5} \mid p_{y,1}\rangle = \langle p_{y,2} \mid p_{y,1}\rangle = \frac{t_{pp\sigma} - t_{pp\pi}}{2}, \qquad \langle p_{z,5} \mid p_{z,1}\rangle = \langle p_{z,2} \mid p_{z,1}\rangle = -t_{pp\pi}, \tag{4.29}$$

and the amplitudes with the opposite sign describing the hopping from a p_y to an e_g orbital on Cr-B:

$$\langle d_{3y^2-r^2,B} \mid p_{y,5}\rangle = -\langle d_{3y^2-r^2,B} \mid p_{y,2}\rangle. \tag{4.30}$$

4.3 Long-range exchange electron interactions

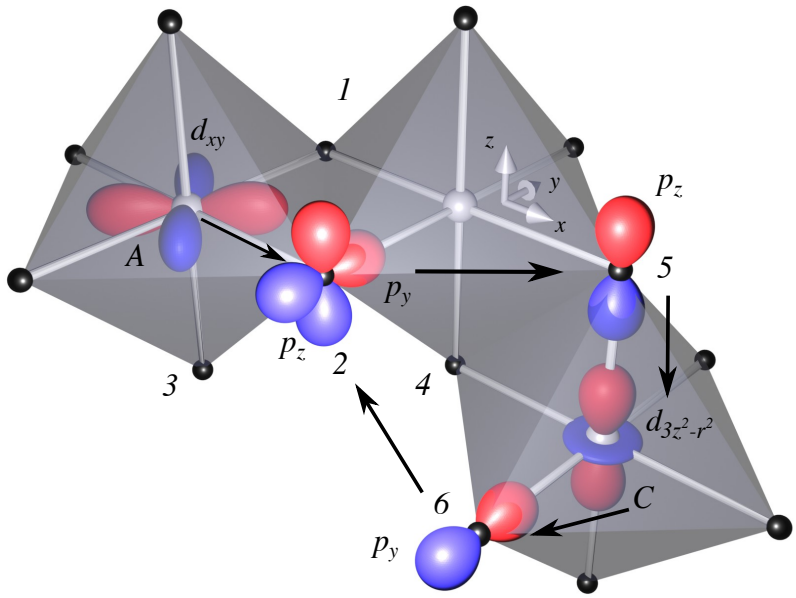

Figure 4.5: ***Three neighboring Cr coordinated by ligand ions and spin-flip electron hoppings between next-nearest-neighboring Cr ions.*** *The diagram shows an exchange path of the electron hopping from the d_{xy} orbital on site A to the $d_{3z^2-r^2}$ orbital on site C. The hopping is due to the coupling between the p_z orbitals of ligand ions 2 and 5, and is preceded by a spin flip on site 2, followed by a change of the orbital state from p_y to p_z. The electron can then hop back to site A via the p_y orbitals of ligand ions 2 and 6. Multiple exchange paths contribute to the effective hopping from a t_{2g} orbital on site A to an e_g orbital on site C due to the hybridization between the p orbitals of ligand ions 1, 2, 3 and 4, 5, 6. The white (black) spheres represent Cr^{3+} (I^-) ions. The red (blue) surfaces of the constant density, $|\Psi(r)|^2$, depict positive (negative) orbital wave functions involved in the exchange process.*

In the previous section, we demonstrated that the electron hopping between ligand ions leads to anisotropic spin interactions described by the Γ term. Additionally, the t_{pp} is responsible for next-nearest-neighbor DMI, which is expected to be proportional to λt_{pp}^2 (see Fig. 4.5 for possible exchange paths). Calculating long-range exchange

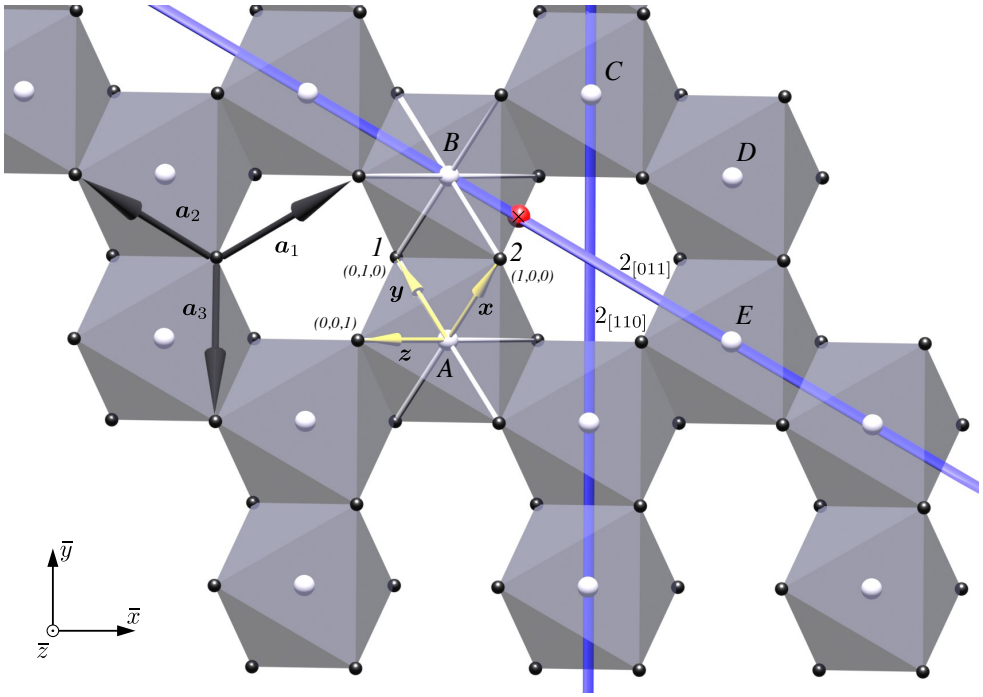

Figure 4.6: ***CrI_3 monolayer crystal structure.*** *The white (black) spheres show Cr^{3+} (I^-) ions. The sublattice of I ions is generated by $\boldsymbol{a}_{1,2,3}$ lattice vectors $\boldsymbol{a}_1 + \boldsymbol{a}_2 + \boldsymbol{a}_3 = 0$ with the unit cell containing two ligand ions 1 and 2. Blue lines show two two-fold rotational symmetry axes of the CrI_3 monolayer: $2_{[110]}$ and $2_{[011]}$, given in the global coordinates $\boldsymbol{x}, \boldsymbol{y}$ and $\boldsymbol{z}$, which are depicted by yellow vectors with length set to one. Other symmetries of the single layer (inversion symmetry center and the third two-fold symmetry axis) are not shown. The crossed red sphere points to the inversion symmetry center of the iodine lattice and two Cr ions A and C. The set of unit vectors $\bar{\boldsymbol{x}}, \bar{\boldsymbol{y}}$ and $\bar{\boldsymbol{z}}$ is the coordinate basis of the monolayer.*

spin-spin interactions is more difficult than nearest-neighbor interactions because of the increasing number of exchange paths involved. The *pp* hopping amplitudes, which are significant [164, 165], cause the delocalization of the ligand hole in the intermediate state over the network of ligand ions. To account for all exchange paths, we utilize a three-step procedure:

1. compute the band states formed by *p*-orbitals of the ligand ions,

2. integrate out the *p* orbitals in the *pd* model to obtain an effective Hamiltonian that describes the long-range electron hoppings between the *d* orbitals of Cr ions,

3. map all possible interactions between Cr spins in second-order perturbation theory in the *dd* hopping amplitude to an effective Hamiltonian that describes spin-spin interactions.

4.3.1 Effective *dd* model

The effective *dd* model can be obtained by integrating out iodine *p* orbitals. The part of the *dd* Hamiltonian is the effective tight-binding *dd* model that describes the electron hopping between two Cr sites A and B,

$$\begin{aligned} H_{dd} = &- |d_B, \boldsymbol{X}_B, \sigma_B\rangle\, t^{\sigma_B\sigma_A}_{d_B,d_A}\left(\boldsymbol{X}_B - \boldsymbol{X}_A\right) \langle d_A, \boldsymbol{X}_A, \sigma_A| \\ &- |d_A, \boldsymbol{X}_A, \sigma_A\rangle \left[t^{\sigma_B\sigma_A}_{d_B,d_A}\left(\boldsymbol{X}_B - \boldsymbol{X}_A\right)\right]^* \langle d_B, \boldsymbol{X}_B, \sigma_B| \,, \end{aligned} \tag{4.31}$$

where $d_A(d_B)$ describes the electron orbital state on a Cr site with coordinate $\boldsymbol{X}_A(\boldsymbol{X}_B)$: $d_A(d_B) = \{1, 2, 3\}$ for the t_{2g} triplet $\{d_{xy}, d_{yz}, d_{xz}\}$ and $d_A(d_B) = \{4, 5\}$ for the e_g doublet $\{d_{x^2-y^2}, d_{3z^2-r^2}\}$, and $\sigma_{A,B}$ are the electron spin projections. This Hamiltonian depends on the total spin of four-electron in an intermediate state. The contributions to spin-spin interactions from the $S = 1$ and $S = 2$ intermediate states decouple and can be summed up independently. The subindex S is omitted in this section for brevity.

The effective *dd* hopping amplitudes in second-order perturbation in the *dp* hopping amplitudes are expressed as:

$$t^{\sigma_B\sigma_A}_{d_B,d_A}\left(\boldsymbol{X}_B - \boldsymbol{X}_A\right) = \sum_{\boldsymbol{k},n} \frac{\langle d_B, \boldsymbol{X}_B, \sigma_B| H_{dp} |V_{\boldsymbol{k},n}\rangle \langle V_{\boldsymbol{k},n}| H_{dp} |d_A, \boldsymbol{X}_A, \sigma_A\rangle}{\Delta_{\boldsymbol{k},n}}, \tag{4.32}$$

where $V_{\boldsymbol{k},n}$ are eigenvectors in reciprocal space – Bloch states with the wave vector $\boldsymbol{k}$ in the band n, describing p-orbitals of I ions. $\Delta_{\boldsymbol{k},n}$ represents the energy gaps used in the previous sections but with the energy of iodine p-orbitals ε_p replaced by the band energy $(\varepsilon_p)_{\boldsymbol{k},n}$. Here, the state $|V_{\boldsymbol{k},n}\rangle$ is a linear combination of 12 states:

$$|V_{\boldsymbol{k},n}\rangle = \sum_{a,J,J_z} c^{a,J,J_z}_{\boldsymbol{k},n} |\boldsymbol{k}, a, J, J_z\rangle \,, \tag{4.33}$$

where $|\boldsymbol{k}, a, J, J_z\rangle$ describes the SOC-coupled p orbital states of two I ions in the unit cell with sublattice index $a = 1, 2$ of the iodine lattice shown in Fig. 4.6, and $c^{a,J,J_z}_{\boldsymbol{k},n}$ are some constants, which are calculated in the next section. These iodine states can be written in the basis of the decoupled p orbital states (see Appendix 4.8.6),

$$|\boldsymbol{k}, a, J, J_z\rangle = \sum_{\substack{\alpha=x,y,z \\ \sigma=\pm 1/2}} U^{p_\alpha,\sigma}_{J,J_z} |\boldsymbol{k}, a, p_\alpha, \sigma\rangle \,, \tag{4.34}$$

which are given in momentum space:

$$|\boldsymbol{k}, a, p_\alpha, \sigma\rangle = \frac{1}{\sqrt{N}} \sum_i e^{i(\boldsymbol{k}\cdot\boldsymbol{x}_i)} |\boldsymbol{x}_i, a, p_\alpha, \sigma\rangle \,, \tag{4.35}$$

with N being the number of wave vectors in the Brillouin zone. By considering explicitly all possible dp hoppings (see Appendix 4.8.3), it is convenient to rewrite Eq. (4.32) as

$$t_{d_B,d_A}^{\sigma_B\sigma_A}(\boldsymbol{X}_B - \boldsymbol{X}_A) = \frac{1}{N}\sum_{\boldsymbol{k},n} \frac{M_{\boldsymbol{k},n}^{d_B,\sigma_B}(M_{\boldsymbol{k},n}^{d_A,\sigma_A})^*}{\Delta_{\boldsymbol{k},n}} e^{i(\boldsymbol{X}_B-\boldsymbol{X}_A)\cdot\boldsymbol{k}}, \tag{4.36}$$

where the matrix elements $M_{\boldsymbol{k},n}^{d_A,\sigma_A}$ are:

$$M_{\boldsymbol{k},n}^{d_{xy},\sigma} = t_{pd\pi}\langle\sigma,\boldsymbol{k}|\left(\langle p_x,1| - e^{-i(\boldsymbol{a}_1+\boldsymbol{a}_2)\cdot\boldsymbol{k}}\langle p_x,2| + \langle p_y,2| - e^{-i(\boldsymbol{a}_1+\boldsymbol{a}_2)\cdot\boldsymbol{k}}\langle p_y,1|\right)|V_{\boldsymbol{k},n}\rangle \,, \tag{4.37}$$

$$M_{\boldsymbol{k},n}^{d_{yz},\sigma} = t_{pd\pi}\langle\sigma,\boldsymbol{k}|\left(\langle p_z,1| - e^{-i(\boldsymbol{a}_1+\boldsymbol{a}_2)\cdot\boldsymbol{k}}\langle p_z,2| + e^{-i\boldsymbol{a}_1\cdot\boldsymbol{k}}\langle p_y,2| - e^{-i\boldsymbol{a}_2\cdot\boldsymbol{k}}\langle p_y,1|\right)|V_{\boldsymbol{k},n}\rangle \,, \tag{4.38}$$

$$M_{\boldsymbol{k},n}^{d_{xz},\sigma} = t_{pd\pi}\langle\sigma,\boldsymbol{k}|\left(e^{-i\boldsymbol{a}_1\cdot\boldsymbol{k}}\langle p_x,2| - e^{-i\boldsymbol{a}_2\cdot\boldsymbol{k}}\langle p_x,1| + \langle p_z,2| - e^{-i(\boldsymbol{a}_1+\boldsymbol{a}_2)\cdot\boldsymbol{k}}\langle p_z,1|\right)|V_{\boldsymbol{k},n}\rangle \,, \tag{4.39}$$

$$M_{\boldsymbol{k},n}^{d_{x^2-y^2},\sigma} = \frac{\sqrt{3}}{2}t_{pd\sigma}\langle\sigma,\boldsymbol{k}|\left(\langle p_y,1| - e^{-i(\boldsymbol{a}_1+\boldsymbol{a}_2)\cdot\boldsymbol{k}}\langle p_y,2| - \langle p_x,2| + e^{-i(\boldsymbol{a}_1+\boldsymbol{a}_2)\cdot\boldsymbol{k}}\langle p_x,1|\right)|V_{\boldsymbol{k},n}\rangle \,, \tag{4.40}$$

$$\begin{aligned} M_{\boldsymbol{k},n}^{d_{3z^2-r^2},\sigma} =& \frac{1}{2}t_{pd\sigma}\langle\sigma,\boldsymbol{k}|\Big(\langle p_y,1| - e^{-i(\boldsymbol{a}_1+\boldsymbol{a}_2)\cdot\boldsymbol{k}}\langle p_y,2| + \langle p_x,2| - e^{-i(\boldsymbol{a}_1+\boldsymbol{a}_2)\cdot\boldsymbol{k}}\langle p_x,1| \\ & - 2e^{-i\boldsymbol{a}_1\cdot\boldsymbol{k}}\langle p_z,2| + 2e^{-i\boldsymbol{a}_2\cdot\boldsymbol{k}}\langle p_z,1|\Big)|V_{\boldsymbol{k},n}\rangle \,. \end{aligned} \tag{4.41}$$

$\boldsymbol{a}_1$ and $\boldsymbol{a}_2$ are the iodine lattice vectors (see Fig. 4.6).

4.3.2 Electron energy bands of the iodine's p orbitals

Including inter-ligand hopping processes makes the isolated ligand states coupled. The pp Hamiltonian describing electron hopping between p orbitals of two iodine sites a and b is

$$H_{pp} = -|\boldsymbol{x}_b, P_b\rangle\, t_{P_b,P_a}(\boldsymbol{x}_b - \boldsymbol{x}_a)\,\langle\boldsymbol{x}_a, P_a| + \text{h.c.}\,, \tag{4.42}$$

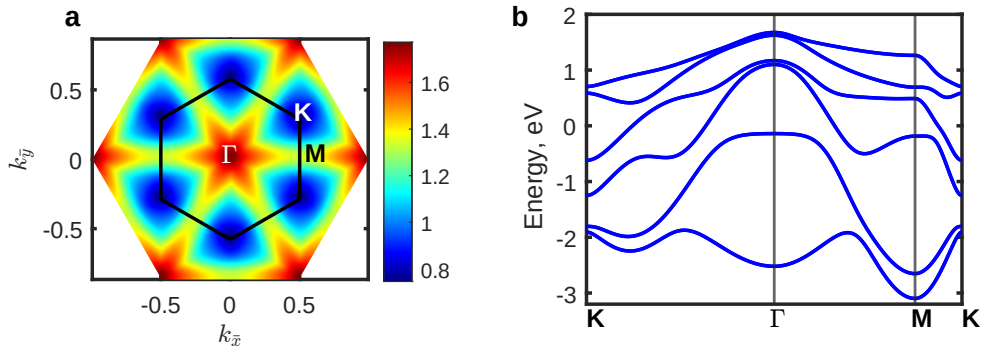

Figure 4.7: ***Iodine energy band structure.*** **a** *Contour plot with color representing the energy of upper lying iodine energy band, given in eV. The black solid line indicates the first Brillouin zone. The lattice constant in the reciprocal space is set to 1. The zero energy corresponds to the energy of p orbital state of isolated iodine. Hopping amplitudes are* $t_{pp\pi} = 0.15$ *eV and* $t_{pp\sigma} = 0.7$ *eV.* **b** *The band structure, shown for high-symmetry lines.*

$P_a(P_b)$ is the 6-dimensional vector describing the orbital state on ligand site $a(b)$ positioned at $\boldsymbol{x}_a(\boldsymbol{x}_b)$: the quadruplet $J = 3/2$ and $J_z = \{3/2, 1/2, -1/2, -3/2\}$, for $P_a = \{1, 2, 3, 4\}$, and the doublet with $J = 1/2$ and $J_z = \{1/2, -1/2\}$, for $P_a = \{5, 6\}$, respectively. The quadruplet energy is $\varepsilon_p + \frac{\lambda}{2}$, and the doublet energy is $\varepsilon_p - \lambda$.

To obtain the matrix elements in Eq. (4.42), we introduce a local coordinate frame with basis unit vectors $\boldsymbol{x}', \boldsymbol{y}', \boldsymbol{z}'$, with $\boldsymbol{z}'$ along the vector connecting two ligand ions. A spin-independent Hamiltonian describing the hopping between the $\{p'_x, p'_y, p'_z\}$ orbitals of the two ions is

$$H'_{pp,0} = -\begin{pmatrix} t_{pp\pi} & 0 & 0 \\ 0 & t_{pp\pi} & 0 \\ 0 & 0 & -t_{pp\sigma} \end{pmatrix}. \tag{4.43}$$

The basis vectors of the local frame can be expressed through those of the global frame by

$$\begin{pmatrix} \boldsymbol{x}' \\ \boldsymbol{y}' \\ \boldsymbol{z}' \end{pmatrix} = R(\theta, \phi) \begin{pmatrix} \boldsymbol{x} \\ \boldsymbol{y} \\ \boldsymbol{z} \end{pmatrix}, \tag{4.44}$$

with

$$R(\theta, \phi) = \begin{pmatrix} \cos\theta\cos\phi & \cos\theta\sin\phi & -\sin\theta \\ -\sin\phi & \cos\phi & 0 \\ \sin\theta\cos\phi & \sin\theta\sin\phi & \cos\theta \end{pmatrix}, \tag{4.45}$$

where θ and ϕ are the polar and azimuthal angles describing the orientation of $\boldsymbol{z}'$.

Hence, in the global coordinates, the *pp* Hamiltonian is

$$H_{pp,0} = R^T H'_{pp,0} R = \\ = -t_{pp\pi} \begin{pmatrix} 1-\alpha\sin^2\theta\cos^2\phi & -\alpha\sin^2\theta\cos\phi\sin\phi & -\alpha\sin\theta\cos\theta\cos\phi \\ -\alpha\sin^2\theta\cos\phi\sin\phi & 1-\alpha\sin^2\theta\sin^2\phi & -\alpha\sin\theta\cos\theta\sin\phi \\ -\alpha\sin\theta\cos\theta\cos\phi & -\alpha\sin\theta\cos\theta\sin\phi & 1-\alpha\cos^2\theta \end{pmatrix}, \quad (4.46)$$

with $\alpha = 1 + \frac{t_{pp\sigma}}{t_{pp\pi}}$. This calculation of the *pp* Hamiltonian is analogous to the Slater-Koster rotated bonds approach [172].

We then add the spin degree of freedom and perform the matrix transformation to the basis of the $|J, J_z\rangle$ state on I sites, as was introduced in Eq (4.34), which leads to the matrix elements in Eq. (4.42). Adding all possible electron hopping processes between nearest-neighbor I ions forming the honeycomb lattice (see Fig. 4.6), including the diagonal matrix that contains the orbital quadruplet and doublet energies, yields the complete Hamiltonian. Its Fourier transform, as given in Eq. (4.35), gives the 12×12 matrix in reciprocal space, which we diagonalize numerically resulting in the eigenstates $|V_{\boldsymbol{k},n}\rangle$ (not shown for brevity) and energy bands shown in Fig. 4.7.

We verified the calculation using a tight-binding model calculating software [175] and analytically checked the results in a limit where $t_{pp\pi} = -t_{pp\sigma}$. This limit effectively transforms the *p*-orbitals into rotationally invariant *s*-orbitals (see Appendix 4.8.7).

4.3.3 Spin Hamiltonian for long-range interactions

We obtain the effective *dd* hopping Hamiltonian in Eq. (4.31) by computing and integrating out the *p*-orbital states. In this section, we finalize the three-step procedure. Namely, we determine the exchange constants in the effective spin Hamiltonian, which describes spin-spin interactions between two Cr ions. We map all possible matrix elements of second-order perturbation theory in *dd* hopping amplitudes to the matrix elements of the spin Hamiltonian. The spin Hamiltonian for two arbitrary Cr ions, A and B, is then given by

$$\begin{aligned} \mathcal{H}_{AB} =& J(\boldsymbol{S}_A \cdot \boldsymbol{S}_B) + \boldsymbol{D}[\boldsymbol{S}_A \times \boldsymbol{S}_B] + K_{zz} S_A^z S_B^z \\ &+ \Gamma_{xy}\left(S_A^x S_B^y + S_A^y S_B^x\right) + \Gamma_{yz}\left(S_A^y S_B^z + S_A^z S_B^y\right) + \Gamma_{zx}\left(S_A^z S_B^x + S_A^x S_B^z\right), \end{aligned} \quad (4.47)$$

where we neglected only $(S_A^x S_B^x - S_A^y S_B^y)$ anisotropy compared to the most general case of a 3×3 spin matrix, describing bilinear spin interactions between two ions.

The Heisenberg exchange coupling is

$$J = \frac{2}{9U_1^{t_{2g}}} \sum_{\substack{d_B \in t_{2g} \\ d_A \in t_{2g}}} \left[\left| t^{\uparrow\uparrow}_{d_B,d_A} \right|^2 + \left| t^{\downarrow\downarrow}_{d_B,d_A} \right|^2 \right]_{S=1} + \sum_{S=1,2} \frac{(-1)^{S+1}}{6U_S^{e_g}} \left[\sum_{\substack{d_B \in e_g \\ d_A \in t_{2g}}} \left| t^{\uparrow\uparrow}_{d_B,d_A} \right|^2 + \sum_{\substack{d_B \in t_{2g} \\ d_A \in e_g}} \left| t^{\downarrow\downarrow}_{d_B,d_A} \right|^2 \right]_S . \tag{4.48}$$

Here, the *dd* hoppings amplitudes are $t^{\sigma_B\sigma_A}_{d_B,d_A}(\boldsymbol{X}_B - \boldsymbol{X}_A)$, with omitted $\boldsymbol{X}_B - \boldsymbol{X}_A$ for brevity compared to the definition in Eq. (4.31). The processes, which contribute to the J coupling, are described in detail in Sec. 4.2.1.

Similarly, the Kitaev exchange coupling (see Sec. 4.2.2) is

$$K_{zz} = -\frac{2}{9U_1^{t_{2g}}} \sum_{\substack{d_B \in t_{2g} \\ d_A \in t_{2g}}} \left[\left| t^{\downarrow\uparrow}_{d_B,d_A} \right|^2 + \left| t^{\uparrow\downarrow}_{d_B,d_A} \right|^2 \right]_{S=1} - \sum_{S=1,2} \frac{(-1)^{S+1}}{6U_S^{e_g}} \left[\sum_{\substack{d_B \in e_g \\ d_A \in t_{2g}}} \left| t^{\downarrow\uparrow}_{d_B,d_A} \right|^2 + \sum_{\substack{d_B \in t_{2g} \\ d_A \in e_g}} \left| t^{\uparrow\downarrow}_{d_B,d_A} \right|^2 \right]_S . \tag{4.49}$$

The xy off-diagonal exchange (see Sec. 4.2.3) coupling is

$$\Gamma_{xy} = \mathrm{Im} \sum_{S=1,2} \frac{(-1)^{S+1}}{6U_S^{e_g}} \left[\sum_{\substack{d_B \in e_g \\ d_A \in t_{2g}}} t^{\downarrow\uparrow}_{d_B,d_A} \left(t^{\uparrow\downarrow}_{d_B,d_A} \right)^* + \sum_{\substack{d_B \in t_{2g} \\ d_A \in e_g}} \left(t^{\uparrow\downarrow}_{d_B,d_A} \right)^* t^{\downarrow\uparrow}_{d_B,d_A} \right]_S . \tag{4.50}$$

We verified that in the limit of zero *pp* hopping amplitudes and for nearest-neighbor Cr ions ($\boldsymbol{X}_B - \boldsymbol{X}_A = \boldsymbol{a}_1 + \boldsymbol{a}_2$), these calculations of $JK\Gamma$ exchange parameters are equivalent to those obtained in Sec. 4.2 with the conventional methods.

The D_z component of the DMI vector is

$$D_z = \mathrm{Im} \sum_{S=1,2} \frac{(-1)^{S}}{6U_S^{e_g}} \left[\sum_{\substack{d_B \in e_g \\ d_A \in t_{2g}}} t^{\uparrow\uparrow}_{d_B,d_A} \left(t^{\downarrow\downarrow}_{d_B,d_A} \right)^* + \sum_{\substack{d_B \in t_{2g} \\ d_A \in e_g}} \left(t^{\downarrow\downarrow}_{d_B,d_A} \right)^* t^{\uparrow\uparrow}_{d_B,d_A} \right]_S . \tag{4.51}$$

This expression is obtained by calculating the imaginary part of the matrix element for the process with the interchange of the spin projections,

$$M^{-+}_{AB} = -\sum_n \left\langle \frac{1}{2}, \frac{3}{2} \right| \frac{H_{dd} \left| n \right\rangle \left\langle n \right| H_{dd}}{E_n} \left| \frac{3}{2}, \frac{1}{2} \right\rangle , \tag{4.52}$$

where $|S_A^z, S_B^z\rangle$ is the state with thebes spin projections S_A^z and S_B^z on sites A and B, and n labels all possible intermediate states with energy E_n. To calculate D_z, we match M_{AB}^{-+} with the matrix element of the effective spin Hamiltonian in Eq. (4.47) with the same initial and final spin projections on sites A and B.

To obtain the exchange constants D_x and D_y together with the Γ_x and Γ_y, we consider processes that lower the spin projection only on site B, such as described by the matrix element:

$$M_{AB}^{z-} = -\sum_n \left\langle \frac{3}{2}, \frac{1}{2} \right| \frac{H_{dd} \left|n\right\rangle \left\langle n\right| H_{dd}}{E_n} \left| \frac{3}{2}, \frac{3}{2} \right\rangle, \tag{4.53}$$

and processes lowering the spin projection only on site A,

$$M_{AB}^{-z} = -\sum_n \left\langle \frac{1}{2}, \frac{3}{2} \right| \frac{H_{dd} \left|n\right\rangle \left\langle n\right| H_{dd}}{E_n} \left| \frac{3}{2}, \frac{3}{2} \right\rangle. \tag{4.54}$$

Calculating these matrix elements in the effective spin model gives the exchange coupling constants:

$$\begin{aligned} D_x &= \frac{2}{3\sqrt{3}} \mathrm{Im}\left(M_{AB}^{-z} - M_{AB}^{z-}\right), \\ \Gamma_x &= \frac{2}{3\sqrt{3}} \mathrm{Im}\left(M_{AB}^{-z} + M_{AB}^{z-}\right), \end{aligned} \tag{4.55}$$

whereas from the real parts of these matrix elements we obtain

$$\begin{aligned} D_y &= -\frac{2}{3\sqrt{3}} \mathrm{Re}\left(M_{AB}^{-z} - M_{AB}^{z-}\right), \\ \Gamma_y &= \frac{2}{3\sqrt{3}} \mathrm{Re}\left(M_{AB}^{-z} + M_{AB}^{z-}\right). \end{aligned} \tag{4.56}$$

The matrix element in Eq. (4.53) is convenient to split in three contributions, $M_{AB}^{z-} = M_{AB,1}^{z-} + M_{AB,2}^{z-} + M_{AB,3}^{z-}$, such that

$$M_{AB,1}^{z-} = \frac{1}{\sqrt{3}} \sum_{S=1,2} \frac{3(-1)^{S+1}}{4U_S^{e_g}} \left[\sum_{\substack{d_B \in e_g \\ d_A \in t_{2g}}} t_{d_B,d_A}^{\downarrow\uparrow} \left(t_{d_B,d_A}^{\uparrow\uparrow}\right)^* \right]_S, \tag{4.57}$$

which describes the spin-up electron that hops from a t_{2g} orbital site A to an e_g orbital on site B with spin flip and returns back to site A in the spin-up state after Hund's rule spin exchange with one of the three electrons on site B. The second term is

$$M_{AB,2}^{z-} = -\frac{1}{\sqrt{3}} \sum_{S=1,2} \frac{(3\delta_{S,1} + \delta_{S,2})}{4U_S^{e_g}} \left[\sum_{\substack{d_B \in t_{2g} \\ d_A \in e_g}} \left(t_{d_B,d_A}^{\uparrow\downarrow}\right)^* t_{d_B,d_A}^{\downarrow\downarrow} \right]_S, \tag{4.58}$$

which describes the spin-up electron that hops from a t_{2g} orbital site B to an e_g orbital on site A with spin flip and returns back to site B in the spin-down state. Here, $\delta_{S,S'}$ is the Kronecker delta function. A similar process with spin-flip occurring on the return of the electron to site B leads to the third matrix element:

$$M^{z-}_{AB,3} = -\frac{1}{\sqrt{3}U_2^{e_g}} \left[\sum_{\substack{d_B \in t_{2g} \\ d_A \in e_g}} \left(t^{\uparrow\uparrow}_{d_B,d_A} \right)^* t^{\downarrow\uparrow}_{d_B,d_A} \right]_{S=2} . \tag{4.59}$$

The matrix elements of the processes that lower the spin projection solely on site A are obtained by analogy, $M^{-z}_{AB} = M^{-z}_{AB,1} + M^{-z}_{AB,2} + M^{-z}_{AB,3}$:

$$M^{-z}_{AB,1} = \frac{1}{\sqrt{3}} \sum_{S=1,2} \frac{3(-1)^{S+1}}{4U_S^{e_g}} \left[\sum_{\substack{d_B \in t_{2g} \\ d_A \in e_g}} \left(t^{\uparrow\downarrow}_{d_B,d_A} \right)^* t^{\uparrow\uparrow}_{d_B,d_A} \right]_S , \tag{4.60}$$

when an electron hops from site B. Two matrix elements when an electron hops from site A are

$$M^{-z}_{AB,2} = -\frac{1}{\sqrt{3}} \sum_{S=1,2} \frac{(3\delta_{S,1} + \delta_{S,2})}{4U_S^{e_g}} \left[\sum_{\substack{d_B \in e_g \\ d_A \in t_{2g}}} t^{\downarrow\uparrow}_{d_B,d_A} \left(t^{\downarrow\downarrow}_{d_B,d_A} \right)^* \right]_S , \tag{4.61}$$

and

$$M^{-z}_{AB,3} = -\frac{1}{\sqrt{3}U_2^{e_g}} \left[\sum_{\substack{d_B \in e_g \\ d_A \in t_{2g}}} t^{\uparrow\uparrow}_{d_B,d_A} \left(t^{\uparrow\downarrow}_{d_B,d_A} \right)^* \right]_{S=2} . \tag{4.62}$$

Contributions to DMI constants from $t_{2g} - t_{2g}$ hopping processes are negligible, hence, they are not shown here.

4.4 Next-nearest-neighbor DMI and magnon Dirac energy gap

4.4.1 The Dirac magnon gap

CrI_3 has been suggested as a promising candidate to host the Kitaev physics, i.e., the model with the K coupling, much larger in magnitude than Heisenberg interactions. However, *the model with strong Kitaev interaction was ruled out* as a scenario to explain the experimentally obtained huge magnon gap at the K point ($\Delta_K \approx 3$ meV [160, 162])

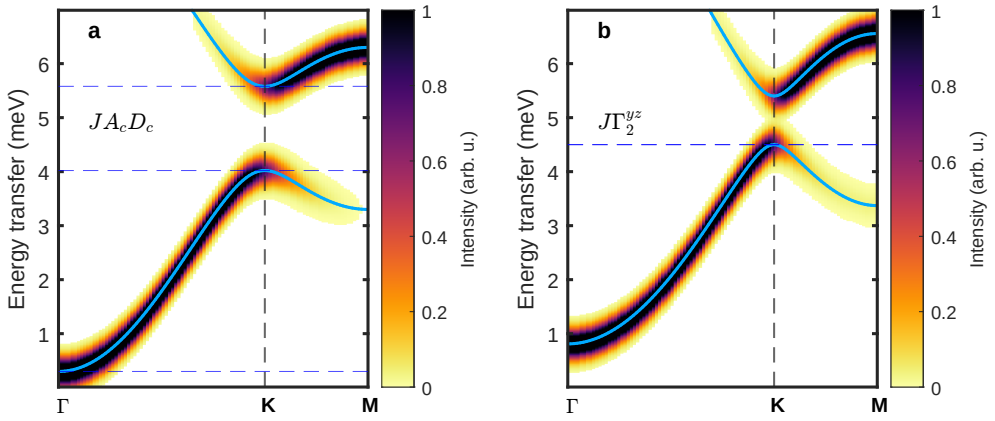

Figure 4.8: ***Typical magnon energy spectra, when one includes interactions that can open the gap at the Dirac*** *K* ***point.*** *The spectra (blue lines) are shown along the high symmetry lines* $\Gamma - K - M$ *in the honeycomb Brillouin zone.* **a** *The magnon spectrum for the* JA_cD_c *model with* $J_1 = -1$ *meV,* $A_c = -0.1$ *meV and* $D_c = 0.1$ *meV, whereas other constants are set to zero. The blue dashed line indicates the analytically calculated energy values at the* Γ *and at the* K *points.* **b** *The magnon spectrum for the* $J\Gamma_2^{yz}$ *model with* $J_1 = -1$ *meV and* $\Gamma_2^{yz} = 0.1$ *meV, whereas other constants are set to zero. The blue dashed line indicates analytically calculated energy value at the* K *point, when* Γ_2^{yz} *is neglected. The black dashed line indicates the* K *point. The spectra are obtained with use of the spinW suite [189]. Pseudo-color coded is the unpolarized neutron scattering cross section (see Ref. [189]), wherein the spectral width is chosen to reproduce the experimental width.*

because the $JK\Gamma$ model failed to describe the magnon spectrum in an in-plane applied magnetic field [160]. In an out-of-plane magnetic field, the experimental magnon spectrum was successfully fitted by the $JK\Gamma$ model [160] giving

$$\begin{aligned} J_1 = -0.83 \text{ meV},\ J_2 = -0.16 \text{ meV},\ J_3 = 0.08 \text{ meV}, \\ K = -3.8 \text{ meV}, \qquad \Gamma = 0.08 \text{ meV}, \end{aligned} \tag{4.63}$$

with J_1(J_2 and J_3) being the nearest- (next-nearest- and third nearest-) neighbor Heisenberg coupling. Note that here we did not show smaller inter-plane Heisenberg exchange coupling and we adapted the sign of the Γ coupling to our choice of the global coordinates. $\Gamma > 0$ corresponds to the easy-axis anisotropy, as addressed in the following section.

The magnon spectrum of the nearest-neighbor $JK\Gamma$ model, including the next-nearest-neighbor DMI with the DMI vector along the out-of-plane direction, was analytically calculated in Ref. [161]. The fact that one needs a large Kitaev coupling is reasonable since at $K < J$, its contribution to the gap is strongly suppressed, as

can be seen from the analytical expressions for the Dirac gap in the $JK\Gamma + D_c$ model:

$$\Delta_K = \omega_{K,+} - \omega_{K,-} = 3S|J| \left(\frac{(2\sqrt{3}}{J} D_c - \left(\frac{2\Gamma + K}{3J} \right)^2 \right) , \tag{4.64}$$

where we expanded to the lowest order in K, Γ and D_c the energies of two magnon branches at the K point, which are given by

$$\begin{aligned} \omega_{K,+} &= S|3J + 2\Gamma + K - 3\sqrt{3}D_c| \,, \\ \omega_{K,-} &= S\sqrt{3J\,(3J + 4\Gamma + 2K) + 18J\sqrt{3}D_c} \,. \end{aligned} \tag{4.65}$$

Equation (4.64) shows that the contribution to the gap is suppressed by $\left(\frac{2\Gamma+K}{J}\right)^2$ for small K and Γ. Additionally, the microscopic analysis in Sec. 4.2 provides no reasoning for K to be larger than J in CrI_3. Moreover, large K can make the collinear ferromagnetic ground state unstable [171].

4.4.2 DMI as origin of the Dirac magnon gap

Alternatively, *the model with next-nearest-neighbor DMI was proposed as the main mechanism* opening the gap at the K point. However, it requires a relatively large DMI constant, as was shown by fitting the experimental magnon spectrum by the JA_cD_c model [160]:

$$\begin{aligned} J_1 = -2.11 \text{ meV},\ J_2 = -0.11 \text{ meV},\ J_3 = 0.1 \text{ meV}, \\ D_c = 0.09 \text{ meV}, \qquad A_c = -0.12 \text{ meV}, \end{aligned} \tag{4.66}$$

where the single-ion anisotropy is introduced as,

$$\mathcal{H}_{\text{SIA}} = A_c \left(\boldsymbol{S} \cdot \hat{\boldsymbol{c}} \right)^2 , \tag{4.67}$$

with the out-of-plane direction $\hat{\boldsymbol{c}} = \frac{1}{\sqrt{3}} (\hat{\boldsymbol{x}} - \hat{\boldsymbol{y}} + \hat{\boldsymbol{z}})$. The easy-axis anisotropy is given by $A_c < 0$. For a comparison, we can estimate D_c, assuming that the DMI is solely responsible for the K-point gap (≈ 3 meV): $D_c \approx \frac{\Delta_K}{6\sqrt{3}S} \approx 0.19$ meV, if one uses Eq. (4.64). Indeed, equation (4.64) shows that the DMI contribution to the gap is linear in D_c, potentially leading to a large gap opening. To illustrate the gap opening, we show the magnon spectrum in the $J_1A_cD_c$ model in Fig. 4.8 **a**.

Importantly, the crystal symmetry allows for two non-zero DMI constants:

$$\begin{aligned} D_\perp &= \frac{1}{\sqrt{3}} \left(D_x - D_y + D_z \right) = D_c \,, \\ D_\parallel &= \frac{1}{\sqrt{6}} \left(2D_x + D_y - D_z \right) , \end{aligned} \tag{4.68}$$

in the Hamiltonian for next-nearest-neighbor Cr sites (A and C in Fig. 4.6),

$$\mathcal{H}_{NNN} = J_2(\boldsymbol{S}_A \cdot \boldsymbol{S}_C) + \boldsymbol{D}[\boldsymbol{S}_A \times \boldsymbol{S}_C]. \tag{4.69}$$

The DMI vector along a two-fold symmetry axis is zero. It is the two-fold symmetry axis ($2_{[011]}$ in Fig. 4.6) that provides the condition $D_y = -D_z$. In the prior analysis, we have not used $D_\parallel$ since for the magnetization polarized along the c axis, it does not affect magnon spectra in harmonic approximation. However, $D_\parallel$ becomes important when magnetization is inclined (or fully in-plane) in the ground state, and it was employed. The in-plane DMI component was suggested to contribute to the Dirac gap under breaking of the three-fold symmetry along the c axis, but it requires quite high magnitudes of the in-plane DMI ($D_\parallel \approx 0.17$ meV) [160]. Similarly, if the Dirac gap was solely due to D_c, we could expect the smooth gap closing when the magnetization is being inclined [160]. The authors showed that in the DMI model, with large magnitude of the DMI vector, the calculated magnon spectra show the best agreement with the experimental magnon spectra in in-plane applied magnetic fields. However, the DMI model still cannot explain the magnetic field behavior of the Dirac magnon gap. Noticeably, the magnon spectra in zero and 4.5 T in-plane applied field are indistinguishable, apart from the spectral weight, (see Fig. 5 in Ref. [160]) which indicates that the Dirac spin gap originates from *isotropic* interactions, but not from DMI. Isotropic interactions can arise due to interplane Heisenberg interactions or a "hidden" magnetic/electronic/structural order that breaks sublattice symmetry of the Cr honeycomb lattice.

4.4.3 Calculation of the DMI vector

The main motivation for our calculations of long-range spin interactions was to find a source of strong DMI. Strikingly, we found that in our model *all components of the DMI vector are equal to zero.* This subtle cancelation is the result of an inversion symmetry center with the origin in the center of the link (see Fig. 4.6), which does not allow DMI along this link. It is not a symmetry of the CrI_3 monolayer, but the symmetry of the lattice of iodine ions and two individual Cr ions A and C. Hence, it is the symmetry of the problem of dd interactions between these two ions, mediated via the iodine states.

Besides DMI, we found only one magnetic interaction that could open the gap: a next-nearest neighbor Γ_{yz} anisotropic exchange, as illustrated in Fig. 4.8 **b**, which is a part of the symmetric exchange Hamiltonian, expressed as,

$$\begin{aligned}\Delta\mathcal{H}_{NNN} =& K_{xx}S_A^xS_C^x + \Gamma_{2,yz}\left(S_A^yS_C^z + S_A^zS_C^y\right) \\ &+ \Gamma_{2,xz}\left(S_A^zS_C^x + S_A^xS_C^z\right) + \Gamma_{2,xy}\left(S_A^xS_C^y + S_A^yS_C^x\right).\end{aligned} \tag{4.70}$$

The $2_{[011]}$ symmetry implies that $\Gamma_{2,xy} = -\Gamma_{2,xz}$ and allows for different coefficients in front of $S_A^x S_C^x$ and $S_A^y S_C^y + S_A^z S_C^z$, hence, the xx-anisotropy of Kitaev type. However, the calculated values of $\Gamma_{2,yz}$ are typically small to account for the large band splitting at the K point, as will be discussed in detail in Sec. 4.6 (see Fig. 4.11 **b**). The next-nearest-neighbor Kitaev interaction only shifts the energy of the Dirac point but do not open the Dirac gap. Similarly, we found that $\Gamma_{2,xy}$ and $\Gamma_{2,xz}$ interactions do not open the Dirac gap.

4.5 Single-ion anisotropy and magnon energy gap at the Γ point

Remarkably, the inclusion of the *pp* hopping also leads to the second-order single-ion anisotropy, introduced in the previous section. This term is prohibited by the cubic symmetry of the iodine octahedra coordinating individual Cr ions. However, taking into account *pp* hopping between ligand sites lowers the cubic symmetry to the dihedral symmetry of CrI_3 monolayer, even in absence of symmetry allowed lattice distortions. Such an interactions-induced symmetry-breaking mechanism leads to the quadratic single-ion anisotropy, as we show in this section.

4.5.1 Origin of the zone-center magnon energy gap

The gap at the Γ point mainly originates from the off-diagonal symmetric exchange anisotropy and the single-ion anisotropy,

$$\Delta_\Gamma = S\,(3\Gamma - 2A_c)\,, \tag{4.71}$$

where $S = 3/2$ is the spin of Cr^{3+} ion. These two interactions both lead to uniaxial anisotropy along the c-axis in a homogeneous spin state, since $3S_c^2 = S(S+1) - \{S_x, S_y\} - \{S_y, S_z\} + \{S_x, S_z\}$. The same magnetic anisotropy is obtained by adding the Γ term interactions between nearest-neighboring Cr spins in the uniform state along the bonds parallel to the Cr lattice vectors ($\boldsymbol{b}_1 = \boldsymbol{a}_1 - \boldsymbol{a}_2$, $\boldsymbol{b}_2 = \boldsymbol{a}_1 + 2\boldsymbol{a}_2$ and $\boldsymbol{b}_3 = -\boldsymbol{b}_1 - \boldsymbol{b}_2$; see Fig. 4.6). To explain the gap at the Γ point ($\Delta_\Gamma \approx 0.3$ meV [160]) without Γ term would require $A_c = -0.12$ meV according to Eq. (4.71). Similarly, if the gap were to emerge from the Γ term only, one would need $\Gamma = \frac{\Delta_\Gamma}{3S} \approx 0.066$ meV. It can be compared to $\Gamma = 0.08$ meV, if the magnon spectrum is fitted using the $JK\Gamma$ model [160] (also see Eq. (4.63)).

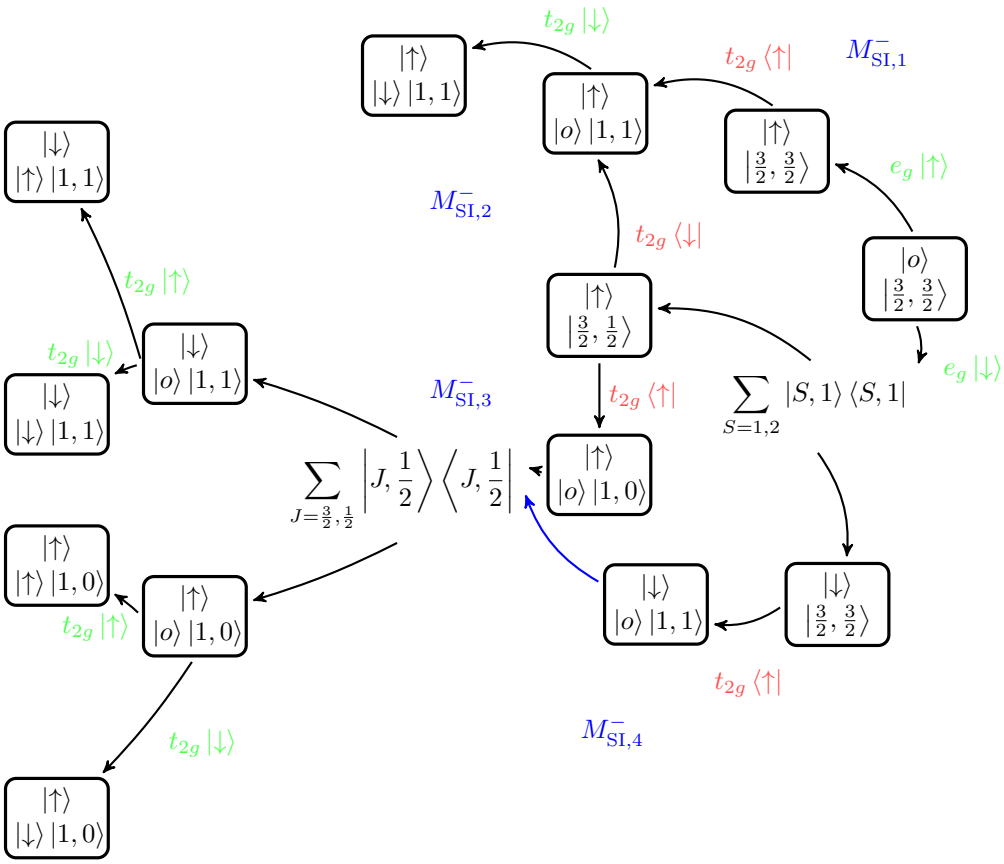

Figure 4.9: ***All possible electron hoppings that lower spin projection on a Cr site.*** *Each block describes the spin state of the Cr ion. The spin state of three (or two) t_{2g}-electrons $|S,S_z\rangle$ is given in the bottom of the block. An empty electron state is identified by $|o\rangle$. The spin projection of an electron on an e_g orbital in an intermediate state is at the top of the block. The initial state with projection $S_z=\frac{3}{2}$ is on the right. Then, each arrow corresponds to a Clebsch-Gordan coefficient, describing the overlap between the product of the initial Cr-state and incoming(outgoing) electron state, depicted with green(red) color. The five final states are projected onto $\left|\frac{3}{2},\frac{1}{2}\right\rangle$ Cr-state, as described in the main text.*

4.5.2 The single-ion anisotropy constant

The single-ion anisotropy is obtained by calculating the matrix element of lowering the spin projection on site A,

$$M^-_{\mathrm{SI}}=-\sum_n\left\langle\frac{1}{2}\right|\frac{H_{dd}\,|n\rangle\langle n|\,H_{dd}}{E_n}\left|\frac{3}{2}\right\rangle \tag{4.72}$$

where $|S_A^z\rangle$ is the state with the spin projection on site A, and n labels all possible intermediate states with energies E_n. Matching M_{SI}^- with the matrix element from the single-ion anisotropic spin interaction results in

$$A_c(1-i) = \sqrt{3} M_{\mathrm{SI}}^-. \tag{4.73}$$

We can directly adapt the *dd* hopping Hamiltonian in Eq. (4.31) for calculating the single-ion anisotropy by substituting $\boldsymbol{X}_B = \boldsymbol{X}_A$, which leads to an effective single-ion Hamiltonian describing the hopping between orbitals d_A and d_B on the same Cr site,

$$H_{dd}^{\mathrm{SI}} = -\left|d_B, \sigma_B\right\rangle t_{d_B,d_A}^{\sigma_B\sigma_A} \left\langle d_A, \sigma_A\right| . \tag{4.74}$$

Henceforth, the matrix element contains four different contributions, $M_{\mathrm{SI}}^- = M_{\mathrm{SI},1}^- + M_{\mathrm{SI},2}^- + M_{\mathrm{SI},3}^- + M_{\mathrm{SI},4}^-$, which is schematically represented in Fig. 4.9. The processes described by the matrix elements $M_{\mathrm{SI},1}^-$ and $M_{\mathrm{SI},2}^-$ involve the total projection 3/2 in the intermediate states with a single hole on a t_{2g} orbital, in contrast to the projection 1/2 for $M_{\mathrm{SI},3}^-$ and $M_{\mathrm{SI},4}^-$. The first matrix element is

$$M_{\mathrm{SI},1}^- = -\frac{1}{\sqrt{3} U_{3/2}^{e_g}} \sum_{\substack{d_B \in e_g \\ d_A \in t_{2g}}} \left(t_{d_B,d_A}^{\uparrow\uparrow}\right)_{S=2} \left[\frac{3}{4}\left(t_{d_B,d_A}^{\uparrow\downarrow}\right)_{S=2}^{*} + \frac{1}{4}\left(t_{d_B,d_A}^{\uparrow\downarrow}\right)_{S=1}^{*}\right]. \tag{4.75}$$

A spin-up electron hops from a ligand orbital to an e_g orbital on the Cr site. Next, one of the three t_{2g} electrons hops back to the iodine lattice. This t_{2g} hole is filled again with spin-up electron. We project the Cr four-electron spin state onto eigenstates of the operator of their total spin. Lastly, the state is projected on the state of the three electrons with the spin projection, 1/2. The last two steps can be expressed as

$$\left\langle \frac{3}{2}, \frac{1}{2}\right|_{t_{2g}} \langle\uparrow|_{e_g} \sum_{\substack{S=1,2 \\ S_z=1}} \left|S, S_z\right\rangle \left\langle S, S_z\right| = \sum_{S=1,2} \left(\delta_{S,2}\frac{\sqrt{3}}{2} - \delta_{S,1}\frac{1}{2}\right) \left\langle S, 1\right| , \tag{4.76}$$

which results in $M_{\mathrm{SI},1}^-$, employing

$$\langle S, 1|\uparrow\rangle_{e_g} \left(|\downarrow\rangle |1, 1\rangle\right)_{t_{2g}} = \frac{1}{\sqrt{3}} \left(\delta_{S,2}\frac{\sqrt{3}}{2} - \delta_{S,1}\frac{1}{2}\right), \tag{4.77}$$

where we used Eqs. (4.26), (4.27) for the four-electron spin state and expressed the t_{2g} spin state as

$$|\downarrow\rangle |1, 1\rangle = \frac{1}{\sqrt{3}} \left|\frac{3}{2}, \frac{3}{2}\right\rangle + \frac{\sqrt{2}}{\sqrt{3}} \left|\frac{3}{2}, \frac{1}{2}\right\rangle. \tag{4.78}$$

The latter expression is due to the spin wave function decomposition of the three-electron spin state,

$$\begin{aligned}\left|\frac{3}{2},\frac{1}{2}\right\rangle &= \frac{1}{\sqrt{3}}\downarrow|1,1\rangle + \sqrt{\frac{2}{3}}\uparrow|1,0\rangle\,,\\ \left|\frac{1}{2},\frac{1}{2}\right\rangle &= \sqrt{\frac{2}{3}}\downarrow|1,1\rangle - \frac{1}{\sqrt{3}}\uparrow|1,0\rangle\,,\end{aligned} \tag{4.79}$$

Energies of the excited state with two t_{2g} electrons and one e_g electron (U_J with total spin $J = 3/2, 1/2$) are given in Appendix 4.8.3. In the scheme Fig. 4.9, the projection operator in Eq. (4.76) is applied to all final states depicted there.

In other three processes, a spin-down electron hops to an e_g orbital, which is less favorable by the Hund's rule coupling. Thus their contribution to A_c is smaller than the one from $M^-_{\mathrm{SI},1}$. The second process is described by

$$M^-_{\mathrm{SI},2} = -\frac{1}{4\sqrt{3}U^{e_g}_{3/2}}\sum_{\substack{d_B\in e_g\\ d_A\in t_{2g}}}\left[\left(t^{\downarrow\downarrow}_{d_B,d_A}\right)_{S=2} - \left(t^{\downarrow\downarrow}_{d_B,d_A}\right)_{S=1}\right]\left[\frac{3}{4}\left(t^{\uparrow\downarrow}_{d_B,d_A}\right)^*_{S=2} + \frac{1}{4}\left(t^{\uparrow\downarrow}_{d_B,d_A}\right)^*_{S=1}\right], \tag{4.80}$$

The state with the spin-down e_g electron is projected on eigenstates of the total spin of four electrons, using $\sum_{S=1,2}|S,1\rangle\langle S,1|$. This projection gives the factor $\frac{\sqrt{3}}{4}(\delta_{S2} - \delta_{S1})$. As on of the three t_{2g} electrons with spin down hops away to a ligand ion, we end up in the same three-electron excited state as in the calculation of the matrix element $M^-_{\mathrm{SI},1}$. With an additional factor of $1/\sqrt{3}$, due to the overlap: $\langle\frac{3}{2},\frac{1}{2}|\downarrow\rangle|1,1\rangle = 1/\sqrt{3}$ (see Eq. (4.79)), which results in $M^-_{\mathrm{SI},2}$.

The second option is to annihilate the spin-up t_{2g} electron leading to the factor $\langle\frac{3}{2},\frac{1}{2}|\uparrow\rangle|1,0\rangle = \sqrt{2/3}$. The resulting excited spin state is projected on the eigenstate of the total spin, using the wave function decomposition Eq. (4.79) for two t_{2g} and one e_g electron with the total spin projection 1/2. This decomposition leads to two independent contributions to the matrix elements, corresponding to $M^-_{\mathrm{SI},3} = M^-_{\mathrm{SI},3\mathrm{a}} + M^-_{\mathrm{SI},3\mathrm{b}}$. $M^-_{\mathrm{SI},3\mathrm{a}}$ is expressed as

$$\begin{aligned}M^-_{\mathrm{SI},3\mathrm{a}} = -\frac{1}{2\sqrt{2}}\sum_{J=3/2,1/2}\frac{1}{U^{e_g}_J}\left(\frac{2}{3}\delta_{J,3/2} + \frac{1}{3}\delta_{J,1/2}\right)\sum_{\substack{d_B\in e_g\\ d_A\in t_{2g}}}\sum_{S=1,2}[\delta_{S,2} - \delta_{S,1}]\left(t^{\downarrow\uparrow}_{d_B,d_A}\right)_S\\ \sum_{S'=1,2}\left[\delta_{S',2}\left(\frac{3}{4} + \frac{1}{\sqrt{6}}\right) + \delta_{S',1}\left(\frac{1}{4} - \frac{1}{\sqrt{6}}\right)\right]\left(t^{\uparrow\uparrow}_{d_B,d_A}\right)^*_{S'}.\end{aligned} \tag{4.81}$$

It describes the diagonal terms after the projection, $\sum_{J=3/2,1/2}|J,1/2\rangle\langle J,1/2|$, which gives rise to the factor $\frac{2}{3}\delta_{J,3/2} + \frac{1}{3}\delta_{J,1/2}$. As the result, we obtain two t_{2g} electrons

in the state $|1,0\rangle$ and the spin-up e_g electron. The t_{2g} vacancy can be filled by an electron with spin-up or spin-down projections. Projecting these two possible states on the final state, as described in Eq. (4.76), one obtains $M^{-}_{\mathrm{SI,3a}}$. Compared to Eq. (4.76), we get a different factor

$$\left\langle \frac{3}{2},\frac{1}{2}\right|_{t_{2g}} \langle\downarrow|_{e_g} \sum_{\substack{S=1,2\\ S_z=0}} |S,S_z\rangle\langle S,S_z| = \frac{1}{2}\sum_{S=1,2}\left(\delta_{S,2}+\delta_{S,1}\right)\langle S,0| \ . \tag{4.82}$$

Intermediate spin states with four electrons on Cr-A with the $S_z=0$ are expressed as,

$$\begin{aligned}
|2,0\rangle &= \frac{1}{\sqrt{2}}\left(\downarrow\left|\frac{3}{2},\frac{1}{2}\right\rangle + \uparrow\left|\frac{3}{2},-\frac{1}{2}\right\rangle\right),\\
|1,0\rangle &= \frac{1}{\sqrt{2}}\left(\downarrow\left|\frac{3}{2},\frac{1}{2}\right\rangle - \uparrow\left|\frac{3}{2},-\frac{1}{2}\right\rangle\right),\\
|0,0\rangle &= \frac{1}{\sqrt{2}}\left(\downarrow\left|\frac{1}{2},\frac{1}{2}\right\rangle - \uparrow\left|\frac{1}{2},-\frac{1}{2}\right\rangle\right).
\end{aligned} \tag{4.83}$$

Note that the processes with the $|0,0\rangle$ intermediate state do not contribute to Eq. (4.82), since they do not survive after the projection onto the final state with the total spin $S=3/2$. Calculation of the remaining matrix elements is analogous to the one discussed above. $M^{-}_{\mathrm{SI,3b}}$ is expressed as

$$\begin{aligned}
M^{-}_{\mathrm{SI,3b}} = -\frac{1}{6}\sum_{J=3/2,1/2}\frac{1}{U^{e_g}_J}\left(\delta_{J,3/2}-\delta_{J,1/2}\right)\sum_{\substack{d_B\in e_g\\ d_A\in t_{2g}}}\sum_{S=1,2}\left[\delta_{S,2}-\delta_{S,1}\right]\left(t^{\downarrow\uparrow}_{d_B,d_A}\right)_S\\
\sum_{S'=1,2}\left[\delta_{S',2}\left(\frac{\sqrt{3}}{4}+\frac{1}{\sqrt{6}}\right)+\delta_{S',1}\left(-\frac{\sqrt{3}}{4}+\frac{1}{\sqrt{6}}\right)\right]\left(t^{\downarrow\downarrow}_{d_B,d_A}\right)^*_{S'}.
\end{aligned} \tag{4.84}$$

For $M^{-}_{\mathrm{SI},4} = M^{-}_{\mathrm{SI,4a}} + M^{-}_{\mathrm{SI,4b}}$, $M^{-}_{\mathrm{SI,4a}}$ is

$$\begin{aligned}
M^{-}_{\mathrm{SI,4a}} = -\sum_{J=3/2,1/2}\frac{1}{U^{e_g}_J}\left(\frac{1}{3}\delta_{J,3/2}+\frac{2}{3}\delta_{J,1/2}\right)\sum_{\substack{d_B\in e_g\\ d_A\in t_{2g}}}\sum_{S=1,2}\left[\frac{1}{4}\delta_{S,2}+\frac{3}{4}\delta_{S,1}\right]\left(t^{\downarrow\uparrow}_{d_B,d_A}\right)_S\\
\sum_{S'=1,2}\left[\delta_{S',2}\left(\frac{\sqrt{3}}{4}+\frac{1}{\sqrt{6}}\right)+\delta_{S',1}\left(-\frac{\sqrt{3}}{4}+\frac{1}{\sqrt{6}}\right)\right]\left(t^{\downarrow\downarrow}_{d_B,d_A}\right)^*_{S'},
\end{aligned} \tag{4.85}$$

and $M^{-}_{\mathrm{SI,4b}}$ is

$$M^{-}_{\mathrm{SI,4b}} = -\frac{\sqrt{2}}{3} \sum_{J=3/2,1/2} \frac{1}{U_J^{e_g}} \left(\delta_{J,3/2} - \delta_{J,1/2}\right) \sum_{\substack{d_B \in e_g \\ d_A \in t_{2g}}} \sum_{S=1,2} \left[\frac{1}{4}\delta_{S,2} + \frac{3}{4}\delta_{S,1}\right] \left(t^{\downarrow\uparrow}_{d_B,d_A}\right)_S \sum_{S'=1,2} \left[\delta_{S',2}\left(\frac{3}{4} + \frac{1}{\sqrt{6}}\right) + \delta_{S',1}\left(\frac{1}{4} - \frac{1}{\sqrt{6}}\right)\right] \left(t^{\uparrow\uparrow}_{d_B,d_A}\right)^*_{S'} . \tag{4.86}$$

Figure 4.10 shows λ- and t_{pp}-dependence of A_c and other calculated spin model parameters.

4.6 Realistic spin model and magnon energy spectrum

We are now in the position to calculate the values of the exchange constants of the spin model and, consequently, the magnon energy spectrum. For our calculations, we used the following hopping amplitudes:

$$t_{pd\sigma} = 1 \text{ eV}, \quad t_{pd\pi} = 0.5 \text{ eV}, \quad t_{pp\sigma} = 0.7 \text{ eV}, \quad t_{pp\pi} = 0.15 \text{ eV}. \tag{4.87}$$

These values are approximately equal to those obtained by *ab initio* calculations by our collaborator Paolo Barone, and details of these calculations will available soon [165]. We rounded the values of the parameters in Eq. (4.87) in order to emphasize that our analysis mainly aims at a qualitative description. The obtained *pd* hopping amplitudes are in good agrement with the corresponding values in Ref. [161], while our *pp* hopping amplitudes are slightly higher than those reported before [164]. However, as discussed in Sec. 4.2.3, *pp* hopping amplitudes can easily be comparable in magnitude with the *pd* amplitudes. The *ab initio* analysis shows better agreement with qualitative estimations [165] using Harrisson's parametrization [166]. The Hubbard constant is $U = 3$ eV, the crystal field splitting energy is $\Delta_c = 1$ eV, and the SOC on iodine sites is $\lambda = 0.63$ eV. These *dp* model parameters are consistent with those used in earlier *ab initio* studies [167–170]. Δ_c corresponds to the energy of the *dd* electron transition between Cr t_{2g} and e_g orbitals and thus can be attributed to the experimentally observed photoluminescence peak at 1.1 eV [173, 174].

We have to define three additional microscopic parameters that describe electron-electron interactions. Estimating these parameters typically requires more sophisticated *ab initio* methods. The first remaining parameter is the Hund's rule coupling, which we keep as a free parameter, yet, assuming values around $J_{\mathrm{H}} \approx 0.24\,U$, as suggested by using constrained random phase approximation (cRPA) [168]. The second Kanamori

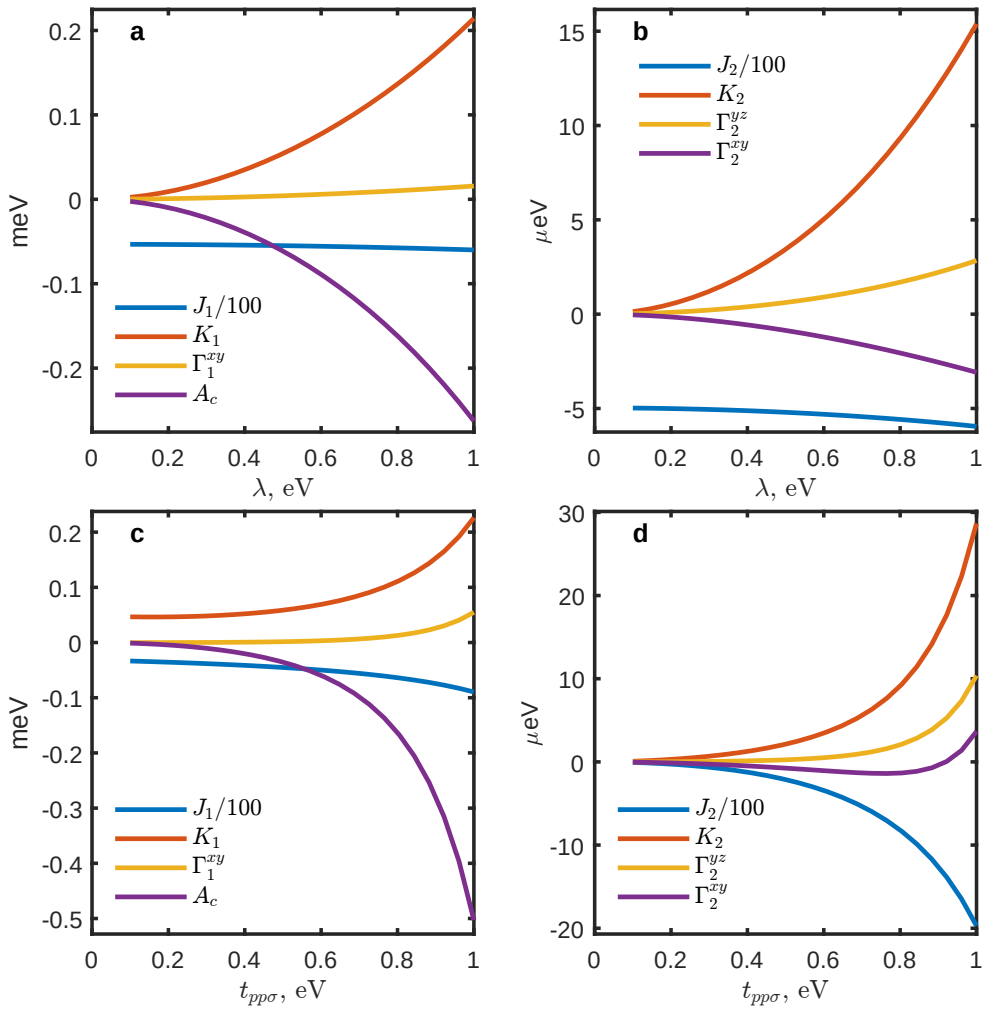

Figure 4.10: ***Spin model parameters.*** **a** *SOC-dependence of the single-ion anisotropy* A_c *and* $JK\Gamma$ *parameters for nearest-neigbor Cr ions and* **b** *next-nearest-neigbor Cr ions.* **c** *pp-hopping amplitude dependence of the single-ion anisotropy* A_c *and* $JK\Gamma$ *parameters for nearest-neigbor Cr ions and* **d** *next-nearest-neigbor Cr ions. In panels* **a,b**, $t_{pp\sigma} = 0.7$ *eV and in panels* **c,d**, $\lambda = 0.63$ *eV. Other microscopic model parameters are:* $t_{pp\pi} = t_{pp\sigma}/4$, $t_{pd\sigma} = 1$ *eV*, $t_{pd\pi} = 0.5$ *eV* $U = 3$ *eV*, $J_{\mathrm{H}} = 0.25U$, $\Delta_c = 1.1$ *eV and* $U' = U - 2J_{\mathrm{H}}$.

parameter is U'. We assume the spherical symmetry, leading to $U' = U - 2J_{\mathrm{H}}$. Note that we checked our analysis for $U = 2$ eV and $U = 4$ eV and found that the final results do not strongly depend on the value of U. Naturally, U can be used as the

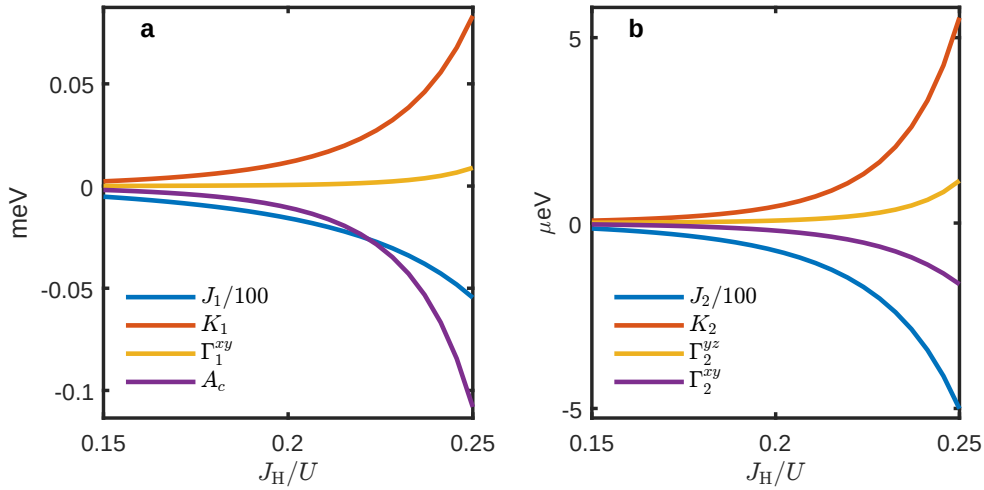

Figure 4.11: ***Spin model parameters dependence on Hund's rule coupling strength.*** **a** *$JK\Gamma$ parameters for nearest-neigbor Cr ions and the single-ion anisotropy A_c.* **b** *$JK\Gamma$ parameters for next-nearest-neigbor Cr ions.*

energy scale for the Kanamori parameters.

By now, we discussed all parameters describing electron-electron correlations on a single Cr site. The last remaining parameter describes electron-electron correlations on an iodine site. Its necessity can be understood by considering the charge-transfer energy, which is a minimum energy required to transfer an electron from I site to Cr site, given by

$$\Delta_{\mathrm{CT}} = \min(\Delta^{e_g}_{S=2})_{\boldsymbol{k}} = \varepsilon_{e_g} - \max(\varepsilon_p(\boldsymbol{k})) + 3U^{'} - 3J_{\mathrm{H}}. \tag{4.88}$$

Here, $\max(\varepsilon_p(\boldsymbol{k}))$ is the highest energy value of the valence band of iodine p electrons, which is at the Γ point (see Sec. 4.3.2). To include interactions on ligand ions in our model, we add $-U_p$ to energies of all intermediate single-hole states. For instance, we replace $\Delta_{\mathrm{CT}} \to \Delta_{\mathrm{CT}} - U_p$ that modifies Eq. (4.88):

$$\Delta_{\mathrm{CT}} = \Delta E_{e_g p} + 3U^{'} - 3J_{\mathrm{H}}, \tag{4.89}$$

where the modified pd energy difference is

$$\Delta E_{e_g p} = \varepsilon_{e_g} - \max(\varepsilon_p(\boldsymbol{k})) - U_p. \tag{4.90}$$

$U_p > 0$ is the Coulomb interaction energy difference between six and five electrons on I site, $U_p = U(6 \text{ electrons}) - U(5 \text{ electrons})$. Its positive sign implies Coulomb repulsion between electrons that favours the five electron state. Similarly to Cr sites,

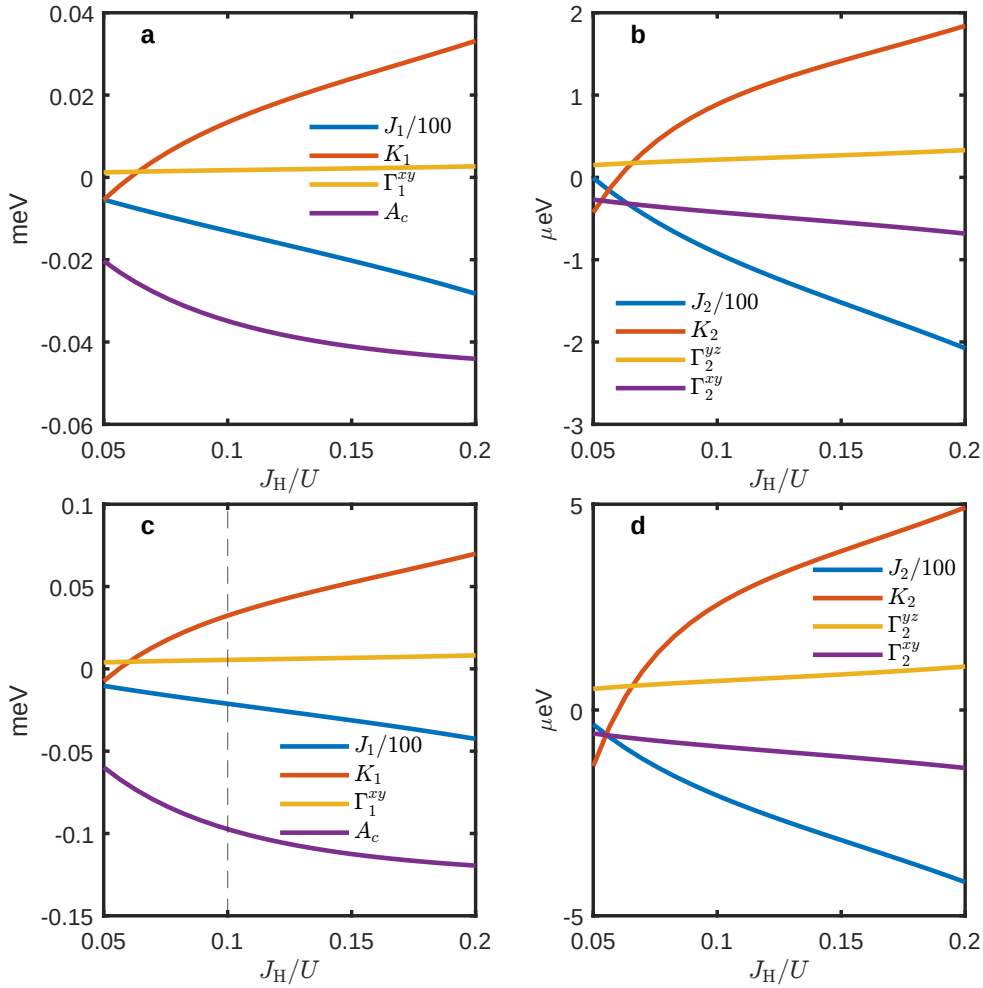

Figure 4.12: ***Spin model parameters dependence on the Hund's rule coupling strength.*** **a, c** *$JK\Gamma$ parameters for nearest-neigbor Cr ions and the single-ion anisotropy A_c.* **b, d** *$JK\Gamma$ parameters for next-nearest-neigbor Cr ions. In* **a, b** *columns, $\Delta_{CT} = 2$ eV. In* **c, d** *columns, $\Delta_{CT} = 1.5$ eV.*

U_p can be expressed via Kanamori parameters on iodine sites (see Appendix 4.8.3), which is not done since all intermediate states in our model can be described by a single parameter U_p. The reason of introducing U_p is to identify $\Delta_{\mathrm{CT}} = 2$ eV with the energy 2 eV of the strong light absorption peak [173, 174]. We found that within the range of parameters presented above, this matching with the experimental data cannot be done consistently, by using free electron energies solely. In contrast, under

condition

$$\varepsilon_{t_{2g}} - \varepsilon_p^{(0)} \approx U_p, \tag{4.91}$$

where $\varepsilon_p^{(0)}$ is the energy of localized p electrons (see the zero energy level in Fig. 4.7), we obtain the correct charge-transfer insulator behaviour of CrI_3 with $\Delta_{\rm CT} \sim 2$ eV. It consistently leaves intact the free energy electronic p and d levels obtained in *ab initio* studies.

First, we set U_p such that it leads to $\Delta E_{e_g p} = -0.23U$, which corresponds to $\Delta_{CT} = 2$ eV at $J_{\rm H}/U = 0.24$. Figure 4.11 shows $J_{\rm H}/U$-dependence of spin model parameters for (panel **a**) nearest-neighbor and for (panel **b**) next-nearest-neighbor (sites A and E in Fig. 4.6) Cr ions. We observe, the sizable single-ion anisotropy that reaches $A_c \approx -0.1$ meV value around the point $J_{\rm H}/U = 0.25$. This value is comparable to the experimental one (see Sec. 4.5 and Ref. [160]). We also find the sizeable Kitaev interaction, comparable in magnitude to the values of A_c. By contrast, the strength of the Γ and the nearest-neighbor anisotropic exchange interactions is too small, which makes these interactions irrelevant. The value of the Heisenberg exchange is too large (~ -5 meV), leading to a much larger magnon band width than the one observed in experiment. Note that in Fig. 4.11, Δ_{CT} varies from 4.2 eV to 1.6 eV as $J_{\rm H}/U$ changes from 0.15 to 0.25, which makes it difficult to separate the effects of Δ_{CT} and $J_{\rm H}$ on spin-spin interactions.

In the second approach, we set Δ_{CT} constant but let the less-known variable U_p vary. For $\Delta_{CT} = 2$ eV, the resulting $J_{\rm H}/U$ of the spin model parameters is shown in Fig. 4.12 (panels **a, b**), wherein $\Delta E_{e_g p}/U$ varies from -1.8 to -0.5 from the smallest to the highest values of $J_{\rm H}$, respectively. In the plot, J's show the linear dependence in $J_{\rm H}$, as was predicted in Sec. 4.2.1 , whereas the dependence of A_c is non-monotonic. Therefore, we repeated the analysis taking a smaller value $\Delta_{CT} = 1.5$ eV that is presented in Fig. 4.12 (panels **c, d**), wherein $\Delta E_{e_g p}/U$ varies from -2 to -0.7. For this value of Δ_{CT} and at $J_{\rm H}/U = 0.1$, our spin model parameters are

$$J_1 = -2.12 \ \text{meV}, \quad J_2 = -0.2 \ \text{meV}, \quad J_3 = 0.005 \ \text{meV}, \quad A_c = -0.1 \ \text{meV}, \tag{4.92}$$

in good agreement with the experimentally obtained values [160]:

$$J_1 = -2.11 \ \text{meV}, \quad J_2 = -0.11 \ \text{meV}, \quad J_3 = 0.1 \ \text{meV}, \quad A_c = -0.12 \ \text{meV}, \tag{4.93}$$

The calculation of the third-nearest-neighbor Heisenberg interaction J_3 (not shown here) is straightforward. It explains the positive J_3 deduced from experiments. However, the strength of the calculated interaction is significantly smaller the experimental value. We found that for the microscopic parameters used to obtained Eq. (4.92), the contributions to J_3 from the $t_{2g} - t_{2g}$ and $t_{2g} - e_g$ hopping channels are both of ~ 0.1 meV, as found in experiment (see Eq.(4.93)), but they almost cancel each other. Notably, the most recent *ab initio* results [169] predict similar smaller values of the

Hund's rule coupling strength ($J_H/U \sim 0.11$), using the cRPA methods that include environmental screening effects. Figure 4.13 shows the resulting magnon spectrum.

Although our calculated magnon spectrum (hence, magnetic parameters) shows the remarkable agreement with the experiments, reflected in the correct slope, i.e., magnon band width mainly defined by the $J_{1,2,3}$ couplings, and the consistent value of the gap at the Γ point (due to A_c), our model cannot explain the reported large Dirac gap. The absence of the DMI due to inversion symmetry of the iodine lattice is discussed in Sec. 4.4, where we also pointed out that $\Gamma_{2,yz}$ can lead to the gap opening at the K point. However, the calculated $\Gamma_{2,yz}$ is too small to explain the large Dirac gap. We found that its contribution to the gap is comparable to the contribution from the nearest-neighbor Kitaev interaction.

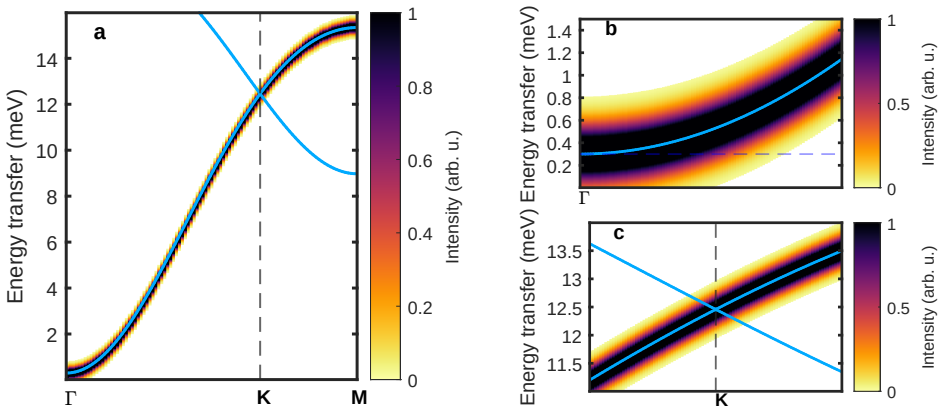

Figure 4.13: ***Magnon energy spectrum for realistic spin model parameters.*** **a** *The spectrum (blue lines) is shown along the high symmetry lines* $\Gamma - K - M$ *in the honeycomb Brillouin zone. The model parameters are* $J_1 = -2.12$ *meV,* $J_2 = -0.2$ *meV,* $J_3 = 0.005$ *meV,* $A_c = -0.1$ *meV and* $K_1 = 0.04$ *meV, whereas other constants are set to zero. The black dashed line indicates the* K *point.* **b** *The zoomed-in spectrum in the vicinity of the* Γ *point. The blue dashed line indicates the analytically calculated energy gap at the* Γ *point (0.3 meV).* **c** *The zoomed-in spectrum in the vicinity of the* K *point. The spectra are obtained with use of the spinW suite [189]. Pseudo-color coded is the unpolarized neutron scattering cross section (see Ref. [189]), wherein the spectral width is chosen to reproduce the experimental width.*

4.7 Discussion

We studied spin-spin interactions in the microscopic *dp* model of CrI_3, which includes the electron hopping between ligand ions. We confirmed that the second-order single-

ion anisotropy is the main source of the magnon energy gap in the Brillouin zone center. We also rule out Kitaev and next-nearest-neighbor DMI scenarios of the experimentally observed large gap at the Dirac point. Whereas the issues with the Kitaev scenario were already well understood [160], the fact that DMI is zero in trigonal distortion-free CrI_3 has not been pointed out before. Small distortions cannot result in DMI with the large magnitude required to explain the gap, since DMI is already suppressed by $\frac{t_{pp}^2}{t_{dd}\Delta}$. To our knowledge, large distortion renormalizing DMI that can explain the gap has not been reported in CrI_3. If the third Cr ion is included in the exchange path, the inversion symmetry will be broken leading to a potential contribution to DMI. However, this contribution is expected to be negligible, since one t_{pp} factor in the expression for the DMI strength will be replaced by t_{pd}^2/Δ_S. The experimentally found magnon gaps for the magnetization vector parallel and perpendicular to the ab plane are nearly the same [160], hinting that the gap at the K point does not originate from anisotropic interactions at all, in contrast to the gap at the Γ point. It indicates that the Dirac gap might originate from symmetric Heisenberg exchange interactions acting non-equivalently within two sublattices. A possible candidate for that is the interlayer exchange interactions, as they are very sensitive to structural changes. Substantial enhancement of interlayer exchange interactions due to electron correlations was discussed in Ref. [176], which leads to a shift of the Dirac point from the high symmetry lines. However, such a scenario was also ruled out in Ref. [160], which proved a "true" gap opening but not the shift of the Dirac point. Such a gap requires the sublattice symmetry breaking, calling for further studies of symmetry-breaking induced by interlayer exchange interactions. In the CrI_3 honeycomb model, the sublattice symmetry is TP, where T is time reversal symmetry and P is inversion symmetry. Van der Waals materials are known to suffer from layer stacking disorder. A single static realization of such disorder in the interlayer Heisenberg interactions can break inversion symmetry. However, inversion symmetry will stil hold on average. In this case, one would only expect large broadening of magnon spectra, which would fill the gap between the acoustic and optical magnon branches.

There are other mechanisms for gap opening at the K point: (i) strong hybridization with phonons and (ii) a "hidden" non-trivial ground state breaking sublattice symmetry, such as a charge density wave or an admixture of antiferromagnetic order due to small spin canting that would require lower symmetry. However, none of them are supported by experimental evidence. Missing in our work are bi-quadratic interactions, which were successfully employed to explain critical behavior in CrI_3 [177, 178]. That is because we did calculations to second order in t_{dd}, and bi-quadratic interactions might appear in the 4-th order. It is unclear how they could contribute to the gap opening.

Two points are essential to our analysis: (i) strong SOC on ligand ions and interligand hopping processes, and (ii) the hierarchy of symmetries and their interrelations.

The cubic symmetry of ligand octahedra coordinating Cr ions is lowered to the symmetry of the Cr-I-Cr-I plaquette, then to monolayer symmetry (dihedral point group D_{3d}). Finally, with the vertical mirror symmetry broken, to rhombohedral symmetry group $R\bar{3}$ of the bulk crystal. The second-order single-ion anisotropy A_c vanishes due to the cubic symmetry of the perfect octahedron. The Γ term vanishes due to $2_{[110]}T$ symmetry of ideal 90° exchange plaquettes. However, with the hopping between the ligand ions taken into account, we obtained large A_c and a non-zero Γ coupling. For DMI calculations, we observed the relevance of the "hidden" symmetry of iodine lattice plus two Cr ions prohibiting DMI between them. The symmetry-breaking mechanisms will be the future direction of our research, which may explain the observed gap.

In this chapter, we discussed the Dirac gap, proposed to give rise to topological magnon bands, but did not study topology of the iodine p orbital states. Topological Mott insulators [179], distinct from the topological band insulator in non-interacting electron models, were proposed for heavy-metal magnetic materials [180]. A realization of this concept has been recently discussed in the context of the twisted bilayer graphene [181]. Magnets with large SOC in heavy ligand ions, such as CrI_3, can realize topological charge transfer insulators, which calls for studies of the interplay between electron and magnonic topological states in these materials.

The often overlooked inter-ligand hopping processes are important because (i) they are relevant for the interplane exchange, tunable in twisted bilayers of van der Waals materials, and further-neighbor in-plane exchange interactions in frustrated magnets; (ii) they can be manipulated with external strains and applied electric fields; (iii) they can be varied by substitutions of ligand ions providing a new handle to forge exotic magnetic orders. Our calculations can be naturally adapted to other van der Waals ferromagnets, most directly to $CrGeTe_3$/$CrSiTe_3$ [133] with heavy Te ligand ions, where a similar gap hierarchy was reported [182, 183] and large trigonal distortions are observed [184]. Understanding the proper low-energy spin models is imperative for finding magnetic topological defects such as skyrmions in these materials [185, 186]. It can allow for efficient ferroelectric control of magnetism in heterostructures [187, 188], which can be used for spintronic applications.

4.8 Appendix

4.8.1 Symmetry arguments for hopping amplitudes

In the main text, we used symmetry analysis to add the contributions from the exchange paths involving the ligand 1 and 2 ions. Generally, symmetry relations for a dd hopping amplitude are

$$\langle d_B, \sigma_B | \hat{H} | d_A, \sigma_A \rangle = \langle d_B, \sigma_B | U^\dagger \hat{H} U | d_A, \sigma_A \rangle , \tag{4.94}$$

where $d_{A,B}$ are some d orbitals at two Cr ions for an electron hopping from the state with spin projection σ_A on site A to the state with σ_B on site B, and we insert $U^\dagger U$ identity between Hamiltonian and wavefunctions with the unitary matrix U being the symmetry operator so that $U\hat{H}U^\dagger = \hat{H}$. For example, under $2_{[110]}T$ symmetry an effective dd hopping amplitude transforms as

$$\langle d_B, \uparrow | \hat{H} | d_A, \uparrow \rangle = \left\langle d_B^{'}, \uparrow \right| \hat{H} \left| d_A^{'}, \uparrow \right\rangle^* , \tag{4.95}$$

where $d_{A,B}^{'}$ are the corresponding 180-degree rotated orbitals. d orbitals transform as components of a symmetric rank-2 tensor under rotations. The transformation matrix describing the rotation about a vector $\boldsymbol{n}$ through an angle ψ of the spin-1/2 state is

$$U_{\mathbf{n}}(\psi) = e^{-i\frac{\psi}{2}(\mathbf{n}\cdot\boldsymbol{\sigma})}, \tag{4.96}$$

with $\boldsymbol{\sigma}$ being Pauli matrices. In the case of the 180° rotation about the diagonal of the square, $2_{[110]}$, the transformation matrix is

$$U_{[110]}(\pi) = e^{-i\frac{\pi}{2}\left(\frac{\sigma_x+\sigma_y}{\sqrt{2}}\right)} = -i\left(\frac{\sigma_x+\sigma_y}{\sqrt{2}}\right), \tag{4.97}$$

and the transformations of spins are given by

$$U_{[110]}(\pi)|\uparrow\rangle = e^{-i\frac{\pi}{4}}|\downarrow\rangle, \qquad U_{[110]}(\pi)|\downarrow\rangle = -e^{i\frac{\pi}{4}}|\uparrow\rangle. \tag{4.98}$$

Time reversal, $T = i\sigma_y K$ with K being the complex conjugation operator, acts on the spin states as follows

$$T|\uparrow\rangle = -|\downarrow\rangle, \qquad T|\downarrow\rangle = |\uparrow\rangle. \tag{4.99}$$

By combining $2_{[110]}$ and T symmetry transformations given in Eqs. (4.98) and (4.99), one obtains Eq. (4.95) and, similarly, for effective hopping amplitudes with spin flip:

$$\begin{aligned} \langle d_B, \uparrow | \hat{H} | d_A, \downarrow \rangle &= i\langle d_B^{'}, \uparrow | \hat{H} | d_A^{'}, \downarrow \rangle^*, \\ \langle d_B, \downarrow | \hat{H} | d_A, \uparrow \rangle &= -i\langle d_B^{'} \downarrow, | \hat{H} | d_A^{'}, \uparrow \rangle^*. \end{aligned} \tag{4.100}$$

In this way we derive the symmetry relations between the effective hopping amplitudes used in the main text using Eqs. (4.95) and (4.100). For instance, one can obtain Eq. (4.18) in Sec. 4.2.2. The amplitudes of hopping from the Cr-A d_{yz} orbital to the Cr-B d_{xy} ($d_A = d_{yz}, d_B = d_{xy}$) and from the Cr-$A$ d_{xz} orbital to the Cr-B d_{xy} ($d_A^{'} = -d_{xz}, d_B^{'} = d_{xy}$) are related in the following way:

$$t_{B,xy,\uparrow;A,yz,\downarrow} = -i(t_{B,xy,\uparrow;A,xz,\downarrow})^*, \tag{4.101}$$

where $t_{B,xy,\uparrow;A,yz,\downarrow} = \langle d_{xy,B}, \uparrow | \hat{H} | d_{yz,A}, \downarrow \rangle$.

4.8.2 dd amplitudes symmetry

For 180° rotation about the $y+z$ axis, $2_{[011]}$, the spin transformation matrix is

$$U_{[011]}(\pi) = e^{-i\frac{\pi}{2}\left(\frac{\sigma_y+\sigma_z}{\sqrt{2}}\right)} = -i\left(\frac{\sigma_y+\sigma_z}{\sqrt{2}}\right). \tag{4.102}$$

Thus, for the effective dd Hamiltonian of electrons hopping between next-to-nearest neigbors in the matrix form, transformation properties are

$$\begin{aligned}
H_{\uparrow\uparrow} =& \frac{1}{2}R^T_{[011]}\left(H^\dagger_{\uparrow\uparrow} - iH^\dagger_{\uparrow\downarrow} + iH^\dagger_{\downarrow\uparrow} + H^\dagger_{\downarrow\downarrow}\right)R_{[011]}\,,\\
H_{\uparrow\downarrow} =& -\frac{1}{2}R^T_{[011]}\left(iH^\dagger_{\uparrow\uparrow} + H^\dagger_{\uparrow\downarrow} + H^\dagger_{\downarrow\uparrow} - iH^\dagger_{\downarrow\downarrow}\right)R_{[011]}\,,\\
H_{\downarrow\uparrow} =& -\frac{1}{2}R^T_{[011]}\left(-iH^\dagger_{\uparrow\uparrow} + H^\dagger_{\uparrow\downarrow} + H^\dagger_{\downarrow\uparrow} + iH^\dagger_{\downarrow\downarrow}\right)R_{[011]}\,,\\
H_{\downarrow\downarrow} =& \frac{1}{2}R^T_{[011]}\left(H^\dagger_{\uparrow\uparrow} + iH^\dagger_{\uparrow\downarrow} - iH^\dagger_{\downarrow\uparrow} + H^\dagger_{\downarrow\downarrow}\right)R_{[011]}\,.
\end{aligned} \tag{4.103}$$

where $R_{[011]}$ is a five by five matrix in the d orbital space with a t_{2g} block,

$$\begin{pmatrix} 0 & 0 & -1\\ 0 & 1 & 0\\ -1 & 0 & 0\end{pmatrix}, \tag{4.104}$$

and an e_g block,

$$\begin{pmatrix} 1/2 & -\sqrt{3}/2\\ -\sqrt{3}/2 & -1/2\end{pmatrix}. \tag{4.105}$$

Here, we took into account that $2_{[011]}$ rotation also interchanges the site A and C resulting in the hermitian conjugation of the hopping Hamiltonian.

4.8.3 Parameters of dp model

The dp model describes d orbitals of transition metal ions and p orbitals of ligand ions (the parameters for Cr compounds can be found in Ref. [164]). Perturbation theory in hopping amplitudes divided by the Hubbard U and/or charge-transfer energy gives an effective Hamiltonian for spins at cation sites. The exchange constants in the effective spin Hamiltonian are expressed in terms of the energies of virtual electronic states and hopping amplitudes. The relevant amplitudes are: $t_{pd\pi}$ and $t_{pd\sigma}$, describing the hopping between transition metal and ligand sites and $t_{pp\pi}$ and $t_{pp\sigma}$, describing the hopping between two ligand sites. They are shown in Fig. 4.14 and are positive, $t_{pd\sigma} = -V_{pd\sigma} > 0$ and $t_{pd\pi} = V_{pd\pi} > 0$ in the notation of Ref. [172]. For example

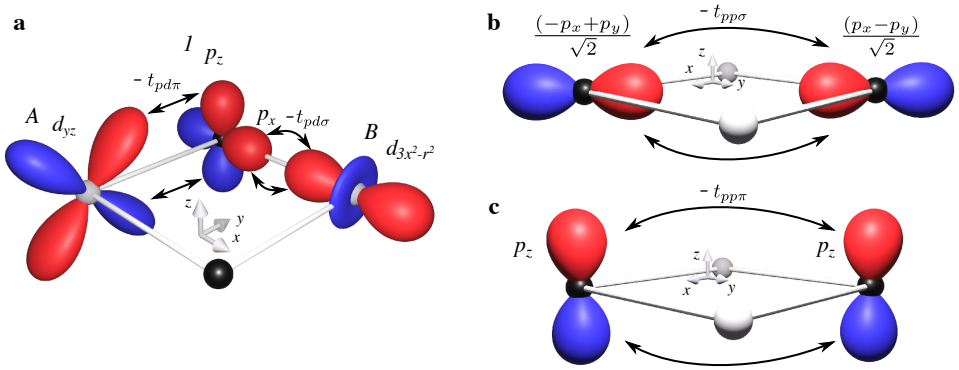

Figure 4.14: ***The hopping amplitudes*** *in the dp model.* **a** *The overlap between the d_{yz} orbital of the metal ion A with the p_z orbital of the ligand ion 1 gives the hopping amplitude $t_{pd\pi}$. The overlap between the p_x orbital and the $d_{3x^2-r^2}$ orbital of the metal ion B gives the amplitude $t_{pd\sigma}$. The overlaps of the p orbitals of the ligands 1 and 2 lead to* **b** *$t_{pp\pi}$ and* **c** *$t_{pp\sigma}$ hopping amplitudes. The white (black) spheres show Cr^{3+} (I^-) ions. The red (blue) surfaces of the constant density, $|\Psi(r)|^2$, depict positive (negative) orbital wave functions.*

the Hamiltonian describing hopping between the $d_{yz,A}$ orbital and the $p_{z,1}$ orbital in Fig. 4.14 is

$$-t_{pd\pi}\Big(|d_{yz,A}\rangle\langle p_{z,1}| + |p_{z,1}\rangle\langle d_{yz,A}|\Big), \tag{4.106}$$

The expressions for energies of the intermediate states for the hopping between t_{2g} orbitals on two Cr sites in terms of the *dp* model parameters are

$$\Delta_{S=1}^{t_{2g}} = \varepsilon_{t_{2g}} - \varepsilon_p + U + 2U^{'}, \qquad U_{S=1}^{t_{2g}} = U + 2J_{\mathrm{H}}, \tag{4.107}$$

where ε_{e_g}, $\varepsilon_{t_{2g}}$ and ε_p are the energies of the respective electronic states, U, $U^{'}$ and J_{H} are the Kanamori parameters describing Coulomb interactions between electrons on transition metal sites [56]: U is the Coulomb repulsion between two electrons occupying the same d orbital, $U^{'}$ is the energy of two electrons at different orbitals with antiparallel spins and $(U^{'} - J_{\mathrm{H}})$ is the Coulomb energy for electrons with parallel spins. The Hund's rule coupling described by the parameter J_{H} gives rise to off-diagonal matrix elements in the Hamiltonian describing electrons on d-sites, i.e., electron pair hopping from one d orbital to another with the amplitude J_{H} and flipping of spins of two electrons with opposite spin projections at two d orbitals with the amplitude $(-J_{\mathrm{H}})$. Δ_S in Eq. (4.107) is the energy of the state with a single hole at a ligand site and the total spin S at the metal site with four electrons, and U_S is the energy of the state with four electrons on one transition metal site and two electrons on the other transition metal site.

The energies relevant for the $e_g - t_{2g}$ hopping processes with the total spin $S = 1, 2$ of four electrons on one Cr ion and two electrons on the second Cr ions in the intermediate state are:

$$\Delta^{e_g}_{S=1} = \varepsilon_{e_g} - \varepsilon_p + 3U^{'} + J_{\mathrm{H}}, \qquad U^{e_g}_{S=1} = \varepsilon_{e_g} - \varepsilon_{t_{2g}} + U^{'} + 3J_{\mathrm{H}}, \tag{4.108}$$

$$\Delta^{e_g}_{S=2} = \varepsilon_{e_g} - \varepsilon_p + 3U^{'} - 3J_{\mathrm{H}}, \qquad U^{e_g}_{S=2} = \varepsilon_{e_g} - \varepsilon_{t_{2g}} + U^{'} - J_{\mathrm{H}}. \tag{4.109}$$

The energies relevant for the $e_g - t_{2g}$ hopping processes with the total spin $S = 1/2, 3/2$ of three electrons on a Cr ion in the first excited states are:

$$U^{e_g}_{S=3/2} = \varepsilon_{e_g} - \varepsilon_{t_{2g}}, \qquad U^{e_g}_{S=1/2} = \varepsilon_{e_g} - \varepsilon_{t_{2g}} + 3J_{\mathrm{H}}. \tag{4.110}$$

It is convenient to write explicitly the *dp* hopping Hamiltonian for arbitrary position of Cr site $\boldsymbol{X}_i$. For the e_g orbitals, the part of H_{dp} describing the electron hopping from a ligand to transition metal ion along the $\hat{\boldsymbol{x}}$ directions (see Fig. 4.6 in the main text) is

$$-t_{pd\sigma}\big(-|p_{x,2,\boldsymbol{X}_i}\rangle + |p_{x,1,\boldsymbol{X}_i-\boldsymbol{a}_1-\boldsymbol{a}_2}\rangle\big)\,\big\langle d_{3x^2-r^2,\boldsymbol{X}_i}\big| + \text{h.c.} \tag{4.111}$$

along the $\hat{\boldsymbol{y}}$ axis,

$$-t_{pd\sigma}\big(-|p_{y,1,\boldsymbol{X}_i}\rangle + |p_{y,2,\boldsymbol{X}_i-\boldsymbol{a}_1-\boldsymbol{a}_2}\rangle\big)\,\big\langle d_{3y^2-r^2,\boldsymbol{X}_i}\big| + \text{h.c.} \tag{4.112}$$

and along the $\hat{\boldsymbol{y}}$ axis,

$$-t_{pd\sigma}\big(-|p_{z,2,\boldsymbol{X}_i-\boldsymbol{a}_1}\rangle + |p_{z,1,\boldsymbol{X}_i-\boldsymbol{a}_2}\rangle\big)\,\big\langle d_{3z^2-r^2,\boldsymbol{X}_i}\big| + \text{h.c.}\,, \tag{4.113}$$

which can be written in terms of the two basis e_g orbitals using Eq. (4.7) in the main text. For t_{2g} orbitals, the part of the H_{dp} hopping Hamiltonian along the $\hat{\boldsymbol{x}}$ direction is

$$\begin{aligned} &-t_{pd\pi}\big(|p_{z,2,\boldsymbol{X}_i}\rangle - |p_{z,1,\boldsymbol{X}_i-\boldsymbol{a}_1-\boldsymbol{a}_2}\rangle\big)\,\langle d_{xz,\boldsymbol{X}_i}| + \text{h.c.} \\ &-t_{pd\pi}\big(|p_{y,2,\boldsymbol{X}_i}\rangle - |p_{y,1,\boldsymbol{X}_i-\boldsymbol{a}_1-\boldsymbol{a}_2}\rangle\big)\,\langle d_{xy,\boldsymbol{X}_i}| + \text{h.c.} \end{aligned} \tag{4.114}$$

the $\hat{\boldsymbol{y}}$ direction,

$$\begin{aligned} &-t_{pd\pi}\big(|p_{z,1,\boldsymbol{X}_i}\rangle - |p_{z,2,\boldsymbol{X}_i-\boldsymbol{a}_1-\boldsymbol{a}_2}\rangle\big)\,\langle d_{yz,\boldsymbol{X}_i}| + \text{h.c.} \\ &-t_{pd\pi}\big(|p_{x,1,\boldsymbol{X}_i}\rangle - |p_{x,2,\boldsymbol{X}_i-\boldsymbol{a}_1-\boldsymbol{a}_2}\rangle\big)\,\langle d_{xy,\boldsymbol{X}_i}| + \text{h.c.} \end{aligned} \tag{4.115}$$

and along the $\hat{\boldsymbol{y}}$ direction,

$$\begin{aligned} &-t_{pd\pi}\big(|p_{y,2,\boldsymbol{X}_i-\boldsymbol{a}_1}\rangle - |p_{y,1,\boldsymbol{X}_i-\boldsymbol{a}_2}\rangle\big)\,\langle d_{yz,\boldsymbol{X}_i}| + \text{h.c.} \\ &-t_{pd\pi}\big(|p_{x,2,\boldsymbol{X}_i-\boldsymbol{a}_1}\rangle - |p_{x,1,\boldsymbol{X}_i-\boldsymbol{a}_2}\rangle\big)\,\langle d_{xz,\boldsymbol{X}_i}| + \text{h.c.}. \end{aligned} \tag{4.116}$$

We can also introduce the Kanamori parameters describing pairwise electron interactions on iodine sites: $U^{(p)}, U'^{(p)}$ and $J^p_{\rm H}$. Then, if neglecting the SOC, the diagonal energy of the fully filled p-shell with 6 electrons is $U(6\text{ electrons}) = 3U^{(p)} + 12U'^{(p)} - 6J^p_{\rm H}$. For a single-hole state with 5 electrons, $U(5\text{ electrons}) = 2U^{(p)} + 6U'^{(p)} - 4J^p_{\rm H}$. The the single parameter describing the electron-electron single-iodine-site interactions U_p, employed in the main text, is given by

$$U_p = U(6\text{ electrons}) - U(5\text{ electrons}) = U^{(p)} + 6U'^{(p)} - 2J^p_{\rm H}. \tag{4.117}$$

4.8.4 Exchange interactions for arbitrary spin projections of Cr ions

Here we discuss the validity of the Heisenberg model for all possible projections of $S = 3/2$ spins of Cr ions. The isotropic exchange interaction J was derived in Sec. 4.2.1 using states with spin projections $\pm 3/2$ of the two Cr metal ions. More generally, the processes that do not change the chromium spin projections, $M'_{A,B} = M_{A,B}$, come with the combination of Clebsch-Gordan coefficients,

$$\sum_\sigma \left[\left(C^{\frac{3}{2},M_A}_{1,M_A-\sigma;\frac{1}{2},\sigma} C^{S,M_B+\sigma}_{\frac{3}{2},M_B;\frac{1}{2},\sigma} \right)^2 + (M_A \leftrightarrow M_B) \right], \tag{4.118}$$

where $\sigma = \pm 1/2$ is the spin projection of the hopping electron, and S is the total spin of the intermediate state with four electrons at a Cr ion. The second term with interchanged M_A and M_B corresponds to the electron hopping in the opposite direction. Both processes are described by the $S^z_A S^z_B$ term of the effective spin Hamiltonian, since the sum over the electron projection σ can be written as

$$\sum_\sigma \left(C^{\frac{3}{2},M_A}_{1,M_A-\sigma;\frac{1}{2},\sigma} C^{S,M_B+\sigma}_{\frac{3}{2},M_B;\frac{1}{2},\sigma} \right)^2 = \frac{1}{2}\left(1 + \frac{(-1)^S}{4} + (-1)^S \frac{M_A M_B}{3} \right), \tag{4.119}$$

where the following relations were used:

$$\left(C^{\frac{3}{2},M_A}_{1,M_A-\sigma;\frac{1}{2},\sigma} \right)^2 = \frac{1}{2} + 2\sigma\frac{M_A}{3}, \tag{4.120}$$

and

$$\left(C^{S,M_B+\sigma}_{\frac{3}{2},M_B;\frac{1}{2},\sigma} \right)^2 = \frac{1}{2}\left(1 + \frac{(-1)^S}{4} \right) + (-1)^S \sigma \frac{M_B}{2}. \tag{4.121}$$

For the same exchange paths but with the spin projections in the final state, $M'_A = M_A - 2\sigma$ and $M'_B = M_B + 2\sigma$, the matrix element of the effective spin Hamiltonian is proportional to

$$\begin{aligned} &C^{\frac{3}{2},M_A}_{1,M_A-\sigma;\frac{1}{2},\sigma} C^{S,M_B+\sigma}_{\frac{3}{2},M_B;\frac{1}{2},\sigma} C^{S,M_B+\sigma}_{\frac{3}{2},M_B+2\sigma;\frac{1}{2},-\sigma} C^{\frac{3}{2},M_A-2\sigma}_{1,M_A-\sigma;\frac{1}{2},-\sigma} \\ &\qquad + C^{\frac{3}{2},M_B}_{1,M_B+\sigma;\frac{1}{2},-\sigma} C^{S,M_A-\sigma}_{\frac{3}{2},M_A;\frac{1}{2},-\sigma} C^{S,M_A-\sigma}_{\frac{3}{2},M_A-2\sigma;\frac{1}{2},\sigma} C^{\frac{3}{2},M_B+2\sigma}_{1,M_B+\sigma;\frac{1}{2},\sigma}. \end{aligned} \tag{4.122}$$

It is proportional to the matrix elements of the $S_A^+ S_B^- + S_A^- S_B^+$ part of the spin Hamiltonian, which was verified for arbitrary M_A, M_B and σ using a Matlab script. Apart from the Clebsch-Gordan coefficients, the pre-factors in front of $S_A^z S_B^z$ and $(S_A^+ S_B^- + S_A^- S_B^+)/2$ are the same (they can be found in Sec. 4.2.1), which shows that our calculation of the exchange interaction J is valid for arbitrary spin projections of Cr ions.

4.8.5 Spin-orbit coupling on ligand sites

The conventional Hamiltonian of the *dp* model is supplemented by a relatively large spin-orbit coupling on ligand ions described by

$$H_{LS} = \lambda \mathbf{L} \cdot \mathbf{S}, \qquad \lambda > 0. \tag{4.123}$$

The energy of *p*-electrons on ligand sites depends on the total angular momentum $\boldsymbol{J} = \boldsymbol{L} + \boldsymbol{S}$:

$$\begin{aligned} \epsilon(J = 3/2) &= \lambda/2, \\ \epsilon(J = 1/2) &= -\lambda, \end{aligned} \tag{4.124}$$

The eigenfunctions $|L, L_z\rangle$ of the orbital momentum,

$$L_j = -i\epsilon_{jkl} r_k \partial_l, \tag{4.125}$$

where ϵ_{jkl} is the Levi-Civita symbol, are

$$\begin{aligned} |1,1\rangle &= -\frac{1}{\sqrt{2}}(p_x + ip_y), \\ |1,0\rangle &= p_z, \\ |1,-1\rangle &= \frac{1}{\sqrt{2}}(p_x - ip_y). \end{aligned} \tag{4.126}$$

This representation simplifies symmetry analysis, since the p_i orbitals transform as the components of a vector under rotations and renders a natural visualization of hopping

processes involving SOC. The eigenstates of J_z and $\mathbf{J}^2$,

$$\begin{aligned}
\left|\frac{3}{2},\frac{3}{2}\right\rangle &= |1,1\rangle\uparrow,\\
\left|\frac{3}{2},\frac{1}{2}\right\rangle &= \frac{1}{\sqrt{3}}|1,1\rangle\downarrow+\sqrt{\frac{2}{3}}|1,0\rangle\uparrow,\\
\left|\frac{3}{2},-\frac{1}{2}\right\rangle &= \sqrt{\frac{2}{3}}|1,0\rangle\downarrow+\sqrt{\frac{1}{3}}|1,-1\rangle\uparrow,\\
\left|\frac{3}{2},-\frac{3}{2}\right\rangle &= |1,-1\rangle\downarrow,\\
\left|\frac{1}{2},\frac{1}{2}\right\rangle &= \sqrt{\frac{2}{3}}|1,1\rangle\downarrow-\sqrt{\frac{1}{3}}|1,0\rangle\uparrow,\\
\left|\frac{1}{2},-\frac{1}{2}\right\rangle &= \frac{1}{\sqrt{3}}|1,0\rangle\downarrow-\sqrt{\frac{2}{3}}|1,-1\rangle\uparrow,
\end{aligned} \tag{4.127}$$

in terms of the p_x, p_y and p_z orbitals are given by

$$\begin{aligned}
\left|\frac{3}{2},\frac{3}{2}\right\rangle &= -\frac{1}{\sqrt{2}}(p_x+ip_y)\uparrow,\\
\left|\frac{3}{2},\frac{1}{2}\right\rangle &= -\sqrt{\frac{1}{6}}(p_x+ip_y)\downarrow+\sqrt{\frac{2}{3}}p_z\uparrow,\\
\left|\frac{3}{2},-\frac{1}{2}\right\rangle &= \sqrt{\frac{2}{3}}p_z\downarrow+\sqrt{\frac{1}{6}}(p_x-ip_y)\uparrow,\\
\left|\frac{3}{2},-\frac{3}{2}\right\rangle &= \frac{1}{\sqrt{2}}(p_x-ip_y)\downarrow,\\
\left|\frac{1}{2},\frac{1}{2}\right\rangle &= -\frac{1}{\sqrt{3}}(p_x+ip_y)\downarrow-\frac{1}{\sqrt{3}}p_z\uparrow,\\
\left|\frac{1}{2},-\frac{1}{2}\right\rangle &= \frac{1}{\sqrt{3}}p_z\downarrow-\frac{1}{\sqrt{3}}(p_x-ip_y)\uparrow.
\end{aligned} \tag{4.128}$$

4.8.6 Diagonalization of Hamiltonian describing one hole on two ligand ions

A correction to the amplitude of electron hopping from the $d_{yz,A}$ orbital to the $d_{3z^2-r^2,B}$ orbital due to hybridization between the ligand p orbitals is

$$\delta t_{B,\downarrow,3z^2-r^2;A,yz,\uparrow} = \sum_{i=1}^{12}\frac{(-1)}{\Delta_i}\langle d_{3z^2-r^2,B}\downarrow|\, H_{dp}\mid V_i\rangle\langle V_i\mid H_{dp}\mid d_{yz,A}\uparrow\rangle, \tag{4.129}$$

where Δ_i are energies of intermediate states discussed in Appendix 4.8.3 but with modified energies of the coupled p orbitals: $\varepsilon_p \to (\varepsilon_p)_i$. V_i and $(\varepsilon_p)_i$ are, respectively,

eigenvectors and eigenstates of the Hamiltonian describing the coupled electron p-orbitals of ligand ions 6 and 7. For such a hybridization, Eq. (4.129) can be expanded to

$$\delta t_{B,\downarrow,3z^2-r^2;A,yz,\uparrow} = t_{pd\sigma}\,(-t_{pd\pi})\sum_{i=1}^{12}\frac{(-1)}{\Delta_i}\langle p_{z,6}\downarrow|\,V_i\rangle\langle V_i\mid p_{y,7}\uparrow\rangle, \tag{4.130}$$

due to hoppings from to the $d_{yz,A}$ to the $p_{y,7}$ orbital and from the $p_{z,6}$ to the $d_{3z^2-r^2,B}$ orbital (see Fig. 4.4 in the main text).

In the basis $\mid J_i\rangle = (\mid J,J_z\rangle_6, \mid J,J_z\rangle_7)^T$, where $\mid J,J_z\rangle_l$ is a column composed of the orbital quadruplet $J=3/2$ and doublet $J=1/2$ on ligand ion l:

$$\left(|3/2,3/2\rangle\,,|3/2,1/2\rangle\,,|3/2,-1/2\rangle\,,|3/2,-3/2\rangle\,,\,|1/2,1/2\rangle\,,|1/2,-1/2\rangle\right)^T, \tag{4.131}$$

the Hamiltonian is a block matrix,

$$H_{pp} = \begin{pmatrix} H_0 & H_{\mathrm{hop,(J)}} \\ H^\dagger_{\mathrm{hop,(J)}} & H_0 \end{pmatrix}, \tag{4.132}$$

where the energies of decoupled ligands are described by

$$H_0 = -\mathrm{diag}(\Delta_{3/2},\Delta_{3/2},\Delta_{3/2},\Delta_{3/2},\Delta_{1/2},\Delta_{1/2}) \tag{4.133}$$

with $\Delta_{3/2} = \Delta_S - \lambda/2$ and $\Delta_{1/2} = \Delta_S + \lambda$. In the basis $\mid J,J_z\rangle$, $H_{\mathrm{hop,(J)}}$ is the Hamiltonian describing the electron hopping between ligands. In the matrix form, $H_{\mathrm{hop,(J)}} = U^\dagger H_{\mathrm{hop,(p)}} U$. Here, $H_{\mathrm{hop,(p)}}$ is the Hamiltonian in the basis $\mid p_i\rangle = (\boldsymbol{p}_7\uparrow,\boldsymbol{p}_7\downarrow,\boldsymbol{p}_6\uparrow,\boldsymbol{p}_6\downarrow)^T$, where $\boldsymbol{p}_l = (p_x,p_y,p_z)^T_l$ is the spin-degenerate orbital triplet on ligand ion l . Hence, $i\in[1,12]$ with $i\in[1,6]$ for ligand ion 7 and $i\in[7,12]$ for ligand ion 6. In the bra-ket notation, the Hamiltonian in the J-basis is

$$\begin{aligned} H_{ij} &= \langle J_i\mid\hat{H}\mid J_j\rangle = \\ &\langle J_i\mid\left(\sum_k\mid p_k\rangle\langle p_k\mid\right)\hat{H}\left(\sum_m\mid p_m\rangle\langle p_m\mid\right)\mid J_j\rangle = \sum_{k,m}U^\dagger_{jk}H_{km}U_{mj} \end{aligned} \tag{4.134}$$

where the matrix elements $U_{ij} = \langle p_i\mid J_j\rangle$ can be found using Eq. (4.128). The spin-independent hopping between ligand ions 6 and 7 is described by

$$H_{\mathrm{hop},0} = -\begin{pmatrix} t_1 & -t_2 & 0 \\ -t_2 & t_1 & 0 \\ 0 & 0 & t_1+t_2 \end{pmatrix}, \tag{4.135}$$

where $t_1 = \frac{-t_{pp\sigma}+t_{pp\pi}}{2}$ and $t_2 = \frac{t_{pp\sigma}+t_{pp\pi}}{2}$. Thus, in the $\mid p_i\rangle$ basis,

$$H^{(p)}_{\mathrm{hop}} = \begin{pmatrix} H_{hop,0} & 0 \\ 0 & H_{hop,0} \end{pmatrix}. \tag{4.136}$$

To this end we solve the Schroedinger equation for one hole on two I ions with the Hamiltonian given in Eq. (4.132),

$$H_{pp} \mid V_i\rangle = (\varepsilon_p)_i \mid V_i\rangle, \tag{4.137}$$

which can be diagonilized exactly. However, it is instructive to obtain linear t_{pp} energy dependence analytically. In this limit, we can consider the σ and π p-orbitals hoppings independently, e.g., by neglecting $t_{pp\pi}$. The problem becomes a single-parameter (the parameter being $t = -t_{pp\sigma}/\Delta_\lambda$) if we subtract $(\varepsilon_p)_{3/2} \mid V_i\rangle$ from both sides of Eq. (4.137) and then divide the equality by $\Delta_\lambda = \Delta_{1/2} - \Delta_{3/2} = \frac{3\lambda}{2}$. Then, as in Eq. (4.129), $\Delta_i = \Delta_{3/2} - \Delta_\lambda \Lambda_i$, where Λ_i for $i \in [5, 12]$ is

$$\begin{pmatrix} \frac{1}{6}(-A_+ - 3t + 3) \\ \frac{1}{6}(-A_+ - 3t + 3) \\ \frac{1}{6}(-A_- + 3t + 3) \\ \frac{1}{6}(-A_- + 3t + 3) \\ \frac{1}{6}(A_+ - 3t + 3) \\ \frac{1}{6}(A_+ - 3t + 3) \\ \frac{1}{6}(A_- + 3t + 3) \\ \frac{1}{6}(A_- + 3t + 3) \end{pmatrix}, \tag{4.138}$$

where $A_\pm = \sqrt{9t^2 \pm 6t + 9}$, and $\Delta_i = \Delta_{3/2}$ for $i \in [1, 4]$. The unnormalized eigenvectors are given in the following matrix with each row representing the eigenvector V_i ($i \in [1, 6]$):

$$\begin{pmatrix} 0 & \frac{i}{\sqrt{3}} & 0 & -\frac{i}{\sqrt{3}} & \frac{i\sqrt{\frac{3}{2}}(-A_- + t - 3)}{4t} & 0 \\ i\sqrt{3} & 0 & -i\sqrt{3} & 0 & 0 & \frac{A_- - t + 3}{4\sqrt{2}t} \\ 0 & -1 & 0 & 1 & \frac{-A_- + t - 3}{4\sqrt{2}t} & 0 \\ -1 & 0 & 1 & 0 & 0 & \frac{i\sqrt{\frac{3}{2}}(-A_- + t - 3)}{4t} \\ 0 & 0 & 0 & 0 & 0 & -1 \\ 0 & 0 & 0 & 0 & -1 & 0 \\ 0 & -\frac{i}{\sqrt{3}} & 0 & -\frac{i}{\sqrt{3}} & \frac{i\sqrt{\frac{3}{2}}(A_- - t + 3)}{4t} & 0 \\ -i\sqrt{3} & 0 & -i\sqrt{3} & 0 & 0 & \frac{-A_- + t - 3}{4\sqrt{2}t} \\ 0 & 1 & 0 & 1 & \frac{A_- - t + 3}{4\sqrt{2}t} & 0 \\ 1 & 0 & 1 & 0 & 0 & \frac{i\sqrt{\frac{3}{2}}(A_- - t + 3)}{4t} \\ 0 & 0 & 0 & 0 & 0 & 1 \\ 0 & 0 & 0 & 0 & 1 & 0 \end{pmatrix} \tag{4.139}$$

and the unnormalized V_i for $i \in [7, 12]$

$$\begin{pmatrix} -\frac{i\sqrt{\frac{3}{2}}\left(A_+ + t + 3\right)}{4t} & 0 & \frac{i\sqrt{\frac{3}{2}}\left(A_- + t - 3\right)}{4t} & 0 & -\frac{i\sqrt{6}\left(-A_+ + t + 3\right)}{8t} & 0 \\ 0 & \frac{A_+ + t + 3}{4\sqrt{2}t} & 0 & -\frac{A_- + t - 3}{4\sqrt{2}t} & 0 & \frac{-A_+ + t + 3}{4\sqrt{2}t} \\ -\frac{A_+ + t + 3}{4\sqrt{2}t} & 0 & \frac{A_- + t - 3}{4\sqrt{2}t} & 0 & \frac{A_+ - t - 3}{4\sqrt{2}t} & 0 \\ 0 & -\frac{i\sqrt{\frac{3}{2}}\left(A_+ + t + 3\right)}{4t} & 0 & \frac{i\sqrt{\frac{3}{2}}\left(A_- + t - 3\right)}{4t} & 0 & -\frac{i\sqrt{6}\left(-A_+ + t + 3\right)}{8t} \\ 0 & 1 & 0 & -1 & 0 & 1 \\ 1 & 0 & -1 & 0 & 1 & 0 \\ -\frac{i\sqrt{\frac{3}{2}}\left(A_+ + t + 3\right)}{4t} & 0 & -\frac{i\sqrt{\frac{3}{2}}\left(A_- + t - 3\right)}{4t} & 0 & -\frac{i\sqrt{6}\left(-A_+ + t + 3\right)}{8t} & 0 \\ 0 & \frac{A_+ + t + 3}{4\sqrt{2}t} & 0 & \frac{A_- + t - 3}{4\sqrt{2}t} & 0 & \frac{-A_+ + t + 3}{4\sqrt{2}t} \\ -\frac{A_+ + t + 3}{4\sqrt{2}t} & 0 & -\frac{A_- + t - 3}{4\sqrt{2}t} & 0 & \frac{A_+ - t - 3}{4\sqrt{2}t} & 0 \\ 0 & -\frac{i\sqrt{\frac{3}{2}}\left(A_+ + t + 3\right)}{4t} & 0 & -\frac{i\sqrt{\frac{3}{2}}\left(A_- + t - 3\right)}{4t} & 0 & -\frac{i\sqrt{6}\left(-A_+ + t + 3\right)}{8t} \\ 0 & 1 & 0 & 1 & 0 & 1 \\ 1 & 0 & 1 & 0 & 1 & 0 \end{pmatrix} \tag{4.140}$$

Similarly, as we neglect $t = -t_{pp\sigma}$ in the beginning, for $t = -t_{pp\pi}/\Delta_\lambda$, $\Delta_i = \Delta_{3/2} - \Delta_\lambda \Lambda_i$, where Λ_i for $i \in [1, 12]$ is

$$\begin{pmatrix} -t \\ -t \\ t \\ t \\ \frac{1}{6}\left(-A_- - 3t + 3\right) \\ \frac{1}{6}\left(-A_- - 3t + 3\right) \\ \frac{1}{6}\left(-A_+ + 3t + 3\right) \\ \frac{1}{6}\left(-A_+ + 3t + 3\right) \\ \frac{1}{6}\left(A_- - 3t + 3\right) \\ \frac{1}{6}\left(A_- - 3t + 3\right) \\ \frac{1}{6}\left(A_+ + 3t + 3\right) \\ \frac{1}{6}\left(A_+ + 3t + 3\right) \end{pmatrix}, \tag{4.141}$$

the unnormalized eigenvectors V_i for $i \in [1,6]$:

$$\begin{pmatrix}
0 & \frac{i}{\sqrt{3}} & 0 & -\frac{i}{\sqrt{3}} & \frac{i\sqrt{\frac{3}{2}}(-A_- +t-3)}{4t} & 0 \\
i\sqrt{3} & 0 & -i\sqrt{3} & 0 & 0 & \frac{A_- -t+3}{4\sqrt{2}t} \\
0 & -1 & 0 & 1 & \frac{-A_- +t-3}{4\sqrt{2}t} & 0 \\
-1 & 0 & 1 & 0 & 0 & \frac{i\sqrt{\frac{3}{2}}(-A_- +t-3)}{4t} \\
0 & 0 & 0 & 0 & 0 & -1 \\
0 & 0 & 0 & 0 & -1 & 0 \\
0 & -\frac{i}{\sqrt{3}} & 0 & -\frac{i}{\sqrt{3}} & \frac{i\sqrt{\frac{3}{2}}(A_- -t+3)}{4t} & 0 \\
-i\sqrt{3} & 0 & -i\sqrt{3} & 0 & 0 & \frac{-A_- +t-3}{4\sqrt{2}t} \\
0 & 1 & 0 & 1 & \frac{A_- -t+3}{4\sqrt{2}t} & 0 \\
1 & 0 & 1 & 0 & 0 & \frac{i\sqrt{\frac{3}{2}}(A_- -t+3)}{4t} \\
0 & 0 & 0 & 0 & 0 & 1 \\
0 & 0 & 0 & 0 & 1 & 0
\end{pmatrix} \tag{4.142}$$

and the unnormalized V_i, $i \in [7,12]$:

$$\begin{pmatrix}
-\frac{i\sqrt{\frac{3}{2}}(A_+ +t+3)}{4t} & 0 & \frac{i\sqrt{\frac{3}{2}}(A_- +t-3)}{4t} & 0 & -\frac{i\sqrt{6}(-A_+ +t+3)}{8t} & 0 \\
0 & \frac{A_+ +t+3}{4\sqrt{2}t} & 0 & -\frac{A_- +t-3}{4\sqrt{2}t} & 0 & \frac{-A_+ +t+3}{4\sqrt{2}t} \\
-\frac{A_+ +t+3}{4\sqrt{2}t} & 0 & \frac{A_- +t-3}{4\sqrt{2}t} & 0 & \frac{A_+ -t-3}{4\sqrt{2}t} & 0 \\
0 & -\frac{i\sqrt{\frac{3}{2}}(A_+ +t+3)}{4t} & 0 & \frac{i\sqrt{\frac{3}{2}}(A_- +t-3)}{4t} & 0 & -\frac{i\sqrt{6}(-A_+ +t+3)}{8t} \\
0 & 1 & 0 & -1 & 0 & 1 \\
1 & 0 & -1 & 0 & 1 & 0 \\
-\frac{i\sqrt{\frac{3}{2}}(A_+ +t+3)}{4t} & 0 & -\frac{i\sqrt{\frac{3}{2}}(A_- +t-3)}{4t} & 0 & -\frac{i\sqrt{6}(-A_+ +t+3)}{8t} & 0 \\
0 & \frac{A_+ +t+3}{4\sqrt{2}t} & 0 & -\frac{A_- +t-3}{4\sqrt{2}t} & 0 & \frac{-A_+ +t+3}{4\sqrt{2}t} \\
-\frac{A_+ +t+3}{4\sqrt{2}t} & 0 & -\frac{A_- +t-3}{4\sqrt{2}t} & 0 & \frac{A_+ -t-3}{4\sqrt{2}t} & 0 \\
0 & -\frac{i\sqrt{\frac{3}{2}}(A_+ +t+3)}{4t} & 0 & -\frac{i\sqrt{\frac{3}{2}}(A_- +t-3)}{4t} & 0 & -\frac{i\sqrt{6}(-A_+ +t+3)}{8t} \\
0 & 1 & 0 & 1 & 0 & 1 \\
1 & 0 & 1 & 0 & 1 & 0
\end{pmatrix} \tag{4.143}$$

Finally, the correction to the hopping amplitude is

$$\delta t_{B,\downarrow,3z^2-r^2;A,yz,\uparrow} = t_{pd\sigma}\,(-t_{pd\pi}) \sum_{i=1}^{12} \frac{(-1)}{\Delta_i} \frac{M_i}{3}, \tag{4.144}$$

where $M_i = 3\langle V_i \mid d_{yz,A}\uparrow\rangle\langle d_{3z^2-r^2,B}\downarrow \mid V_i\rangle$:

$$\begin{aligned} M_i = {} & V_i(9)^* V_i(3) - V_i(12)^* V_i(6) - \sqrt{2} V_i(12)^* V_i(3) \\ & + V_i(9)^* V_i(6)/\sqrt{2} + \sqrt{3} V_i(7)^* V_i(3) + \sqrt{3/2} V_i(7)^* V_i(6) \end{aligned} \tag{4.145}$$

with $V_i(j) = \langle J_j \mid V_i\rangle$. In the limit $t_{pp}/\Delta_S \to 0$,

$$-\sum_i \frac{M_i}{\Delta_i} = \frac{1}{6}\left(\frac{t_{pp\sigma} - 5t_{pp\pi}}{\Delta_{3/2}^2} - \frac{2t_{pp\sigma} - 4t_{pp\pi}}{\Delta_{1/2}^2}\right) + \frac{1}{6}\frac{t_{pp\sigma} + t_{pp\pi}}{\Delta_{3/2}\Delta_{1/2}}, \tag{4.146}$$

which in the limit $\lambda/\Delta_S \to 0$, results in Eq. (4.22) in the main text,

$$\sum_i \frac{M_i}{3\Delta_i} = -\frac{3\lambda}{4\Delta_S^3}\left(3t_{pp\pi} - t_{pp\sigma}\right). \tag{4.147}$$

4.8.7 Diagonalization of ss Hamiltonian

In the main text (Sec. 4.3), the pp Hamlitonian in the global coordinate in Eq. (4.46) becomes effectively diagonal for interaction in an arbitrary pair of ligand ions if one substitutes $t_{pp\pi} = -t_{pp\sigma} = t_{ss}$. This case correspond to a soluble model of electrons hopping between s orbitals of sites i and j described by the Hamiltonian,

$$-t_{ss} H^{ij}_{\alpha,\beta} c^\dagger_{\alpha,i} c_{\beta,j} + \text{h.c.}\,, \tag{4.148}$$

with α (β) indexing the sublattice. In momentum space,

$$\begin{aligned} H^k_{1,1} =& 2\cos\left(\boldsymbol{a}_1\cdot\boldsymbol{k}\right) + 2\cos\left(\boldsymbol{a}_2\cdot\boldsymbol{k}\right) + 2\cos\left(\left(\boldsymbol{a}_1+\boldsymbol{a}_2\right)\cdot\boldsymbol{k}\right), \\ H^k_{1,2} =& 1 + e^{-i\boldsymbol{a}_1\cdot\boldsymbol{k}} + e^{i\boldsymbol{a}_2\cdot\boldsymbol{k}}, \\ H^k_{2,2} =& H^k_{1,1} \quad H^k_{2,1} = \left(H^k_{1,2}\right)^* . \end{aligned} \tag{4.149}$$

The energy is

$$E_k = h^k_0 \pm \sqrt{\left(h^k_x\right)^2 + \left(h^k_y\right)^2}, \tag{4.150}$$

where

$$h^k_0 = H^k_{1,1}\,, \quad h^k_x = \frac{H^k_{1,2} + H^k_{2,1}}{2}\,, \quad h^k_y = -\frac{H^k_{1,2} - H^k_{2,1}}{2i}. \tag{4.151}$$